

**SEARCH FOR TYPE-III SEESAW HEAVY FERMIONS
WITH MULTILEPTON FINAL STATES USING 2.3 fb^{-1}
OF $\sqrt{s} = 13 \text{ TeV}$ PROTON-PROTON COLLISION DATA**

By

PETER THOMASSEN

A dissertation submitted to the
Graduate School—New Brunswick
Rutgers, The State University of New Jersey
in partial fulfillment of the requirements
for the degree of
Doctor of Philosophy
Graduate Program in Physics and Astronomy
written under the direction of
Dr. Sunil Somalwar
and approved by

New Brunswick, New Jersey

May, 2016

© 2016

Peter Thomassen

ALL RIGHTS RESERVED

ABSTRACT OF THE DISSERTATION

Search for Type-III Seesaw Heavy Fermions with Multilepton Final States using 2.3 fb^{-1} of $\sqrt{s} = 13 \text{ TeV}$ proton–proton Collision Data

By PETER THOMASSEN

Dissertation Director:

Dr. Sunil Somalwar

A search for type-III seesaw signal in events with three or more electrons or muons is presented. The data sample corresponds to 2.3 fb^{-1} of integrated luminosity in pp collisions at $\sqrt{s} = 13 \text{ TeV}$ collected by the CMS experiment at the LHC. Since the signal populates channels with at least three leptons and diverse kinematic properties, the data is binned in exclusive channels. The primary selection is based on the number of leptons and the invariant mass of opposite-sign dilepton systems which helps discriminate the signal against the Standard Model background. The final optimization for the type-III seesaw signal is based on the sum of leptonic transverse momenta and missing transverse energy. Control samples in data are used to check the robustness of background evaluation techniques and to minimize the reliance on simulation. The observations are consistent with expectations from Standard Model processes. The results are used to exclude heavy fermions of the type-III seesaw model with masses below 430 GeV.

Acknowledgments

Many individuals and institutions have supported me during my Ph. D. studies and thesis writing. I would like to express my gratitude especially to my supervisor Prof. Sunil Somalwar whose advice and guidance were both extremely valuable and refreshing, and to the members of the research group that I have been part of, especially our postdocs Richard Gray, Matt Walker, and Halil Saka, as well as to my fellow graduate students Sanjay Arora, Christian Contreras-Campaña, Emmanuel Contreras-Campaña, Maximilian Heindl, Shruti Panwalkar, Patrick Zywicki for their helpful discussions, input, and distractions. Special thanks go to Prof. Scott Thomas for his guidance on theoretical matters, to Kevin Feiglis for his support with the signal simulation, to Ezio Torassa and Andrea Gozzelino for the collaboration on the seesaw model, to Nils Wisiol for editorial suggestions, and to my dear fellow student Elliot “Tote” Hughes.

My involvement with Rutgers University started initially with an exchange organized by Würzburg University. Financial support for the exchange was provided by the German Academic Exchange Service (DAAD). Further funds, for travel purposes as well as generally, came from several scholarships of the Foundation of German Business (Stiftung der Deutschen Wirtschaft, sdw), COLA support from the National Science Foundation (NSF), as well as from Rutgers University and Prof. Somalwar’s NSF grant.

This thesis contains material from previous publications that I have authored [1, 2].

Table of Contents

Abstract	ii
Acknowledgments	iii
List of Tables	vii
List of Figures	viii
1. Introduction	1
2. Theoretical Overview	4
2.1. Standard Model	4
2.1.1. Fermions	4
2.1.2. Bosons	7
2.2. Shortcomings of the Standard Model	7
2.3. Type-III Seesaw Mechanism	8
2.3.1. Phenomenology	8
2.3.2. Signal Model and Generation	9
3. Experimental Apparatus	11
3.1. The Large Hadron Collider	11
3.2. The CMS Detector	12
3.2.1. Tracking System	14
3.2.2. Electromagnetic and Hadronic Calorimeter	15

3.2.3. Muon System	17
3.2.4. Trigger and Data Storage	17
4. Datasets and Triggers	20
4.1. Triggers	20
4.2. Background MC samples	20
5. Selection	24
5.1. Object Selection	24
5.1.1. Electrons and Muons	24
5.1.2. Missing Transverse Momentum (E_T^{miss})	27
5.2. Event Selection	27
6. Search Strategy	28
6.1. General Approach	28
6.2. Signal Regions	29
7. Backgrounds	34
7.1. WZ Background	35
7.2. $t\bar{t}$ Background	38
7.2.1. Dilepton Studies	38
7.2.2. Trilepton Studies	41
7.2.3. Dilepton + Track Studies	41
7.3. Z + fake Background	42
7.3.1. Method	42
7.3.2. Fake Leptons from Asymmetric Internal Photon Conversions (AIC)	44
7.3.3. Fake Leptons from Jets	48
7.4. ZZ Background	49

8. Systematic Uncertainties	55
9. Results	57
9.1. Observation	57
9.2. Interpretation for the Seesaw Model	60
9.2.1. Single-channel Limits	60
9.2.2. Multi-channel Limits	61
9.2.3. Full Combination	61
9.3. Cross-checks	63
9.3.1. Back-of-the-Envelope Limits	63
9.3.2. Simplified Limits from Leading Production and Decay Modes	65
9.3.3. Comparison to Run-I Results	65
10. Conclusion	68
Appendix A. Suitability of Tracks as Fake Proxies	69
Appendix B. Analysis Software	71
B.1. RutgersAODReader	71
B.2. EventAnalyzer	71
B.3. AnalysisPresenter	73
B.3.1. Scope and Design Principles	73
B.3.2. Distributions	74
B.3.3. Bundling Mechanism and MC Subtraction	75
B.3.4. Channel Collections and Datacards	76
B.3.5. Runtime	77
Bibliography	78

List of Tables

2.1. Elementary particles in the Standard Model [7, 18, 19]. For electrically charged particles, anti-particles with opposite charge exist. Neutrinos presumably have anti-particles with opposite chirality. Anti-particles have been omitted in this summary.	5
4.1. Data samples.	20
4.2. Background MC samples.	21
5.1. Multi-isolation working points used in the analysis.	26
6.1. Signal Regions. Overlap with control regions removed everywhere.	33
7.1. Background control regions (left) are defined by the criteria listed at the top. S_T is the scalar sum of the lepton transverse momenta, the transverse momenta of jets, and E_T^{miss}	35
8.1. Systematic uncertainties. The channels listed here have three leptons and $550 \text{ GeV} < L_T + E_T^{\text{miss}} < 750 \text{ GeV}$	56
9.1. Relative Sensitivity of Signal Regions.	60
9.2. Most significant trilepton processes with branching ratios to the bosonic level.	64
9.3. Estimate of reconstructed trilepton signal events. The combined leptonic branching ratio of all involved bosons is denoted as BR_{lep}	65
9.4. Sensitivity improvements compared to the Run I analysis.	67

List of Figures

2.1.	Examples of Feynman diagrams for heavy fermion production in the type-III seesaw model.	9
2.2.	Feynman diagram example of the fermion production and decay in the type-III seesaw model.	9
2.3.	Branching ratios from the pair-produced fermions to the bosonic level of the most relevant decay modes.	10
3.1.	CERN Accelerator Complex [40]. The diagram shows the different accelerators, detectors, and other facilities at CERN. For proton collisions, not all of the machinery is needed: Protons are initially accelerated to 50 MeV in a Linear Accelerator (LINAC 2). Then, they are transported to the Booster (1.4 GeV), to the Proton Synchrotron (PS, 25 GeV) and the Super Proton Synchrotron (SPS, 450 GeV) from where they are injected into LHC. The PS also takes care of arranging the protons in bunches with the correct spacing for LHC.	12
3.2.	A transverse slice through CMS [41]. The illustration shows the most important detector components as well as examples of different particles as they are detected while traveling through the detector.	13
3.3.	A module of the electromagnetic calorimeter consisting of 500 lead-tungstate crystals.	16
3.4.	Sketch of the muon system in CMS in r - z view. The drift tubes are displayed in dark-green, the cathode strip chambers in dark-blue, and the resistive plate chambers in dark-red. The light-colored areas are the tracker and calorimeter. The interaction point is located at the origin of the coordinate system.	18

4.1. n_{vertex} distribution for events with at least three light leptons.	23
6.1. $m_{\ell\ell}$ distribution in the dilepton fake region (off-Z, trilepton events with $m_{\ell\ell\ell}$ on Z have been vetoed).	30
6.2. $L_T + E_T^{\text{miss}}$ shape for two different production and decay modes at $m_\Sigma = 340 \text{ GeV}$, with WZ background. Signal normalization arbitrary (for illustration purposes only).	31
6.3. $L_T + E_T^{\text{miss}}$ distribution after event selection cuts from Sec. 5.2, to illustrate the signal separation power of this variable (last bin includes overflow). Backgrounds are described in Chapter 7. The signal ($m_\Sigma = 420 \text{ GeV}$, sum of all production and decay modes) is shown as white square dots with a pink hashed uncertainty band. The background uncertainty is specified by the gray band. Uncertainty bands include both statistical and systematic uncertainties. Numbers in square brackets denote the number of events contributed by each process.	32
7.1. n_{jets} distribution in the WZ-dominated control region (last bin includes overflow). Uncertainty bands include both statistical and systematic uncertainties, with the exception of the WZ normalization uncertainty.	36
7.2. M_T distributions in the WZ-dominated control and validation regions (last bin includes overflow). Uncertainty bands include both statistical and systematic uncertainties, with the exception of the WZ normalization uncertainty.	37
7.3. n_{jets} distributions in $t\bar{t}$ -dominated control region (last bin includes overflow). Uncertainties are statistical only.	39
7.4. Kinematic distributions in $t\bar{t}$ -dominated control region (last bin includes overflow). Uncertainties are statistical only.	40
7.5. Track distributions in $t\bar{t}$ -dominated control region (last bin includes overflow). Uncertainties are statistical only.	43
7.6. ΔR distributions between photon and muon.	46

7.7.	$m_{3\ell}$ distribution in AIC-dominated control region.	47
7.8.	p_T distributions of the lowest p_T lepton.	50
7.9.	$m_{\ell\ell}$ distribution in the dilepton + fake region.	51
7.10.	$m_{\ell\ell}$ distribution in the dilepton + fake region by flavor.	52
7.11.	H_T distribution in the dilepton fake region (no OSSF pair mass cut).	53
7.12.	Closure test in Drell-Yan MC for the track-based fake rate method. The plot compares the 3-lepton yield with the prediction from 2 leptons + track proxy. The second bin in this plot ranges from 101 GeV to infinity.	53
7.13.	The $m_{4\ell}$ distribution in the ZZ control region. The last bin is the overflow. Uncertainty bands include both statistical and systematic uncertainties, with the exception of the ZZ normalization uncertainty.	54
9.1.	Results: $L_T + E_T^{\text{miss}}$ distributions (last bin includes overflow in all plots).	58
9.2.	Event displays for events from Fig. 9.1a.	59
9.3.	Results: Exclusion curves. Masses to the left of the intersection point are excluded.	62
9.4.	Exclusion for the flavor-democratic type-III seesaw model ($V_e = V_\mu = V_\tau = 10^{-6}$). We exclude heavy fermion pair production for masses below $m_\Sigma = 440$ GeV (expected: 430 GeV) and give upper limits on the pair production cross section.	63
9.5.	Exclusion for the flavor-democratic type-III seesaw model using the seven leading signal production/decay modes only.	66
9.6.	Bins of lepton charge sum used in mock-up Run I result, with 13 TeV dataset and background estimates (3 leptons only).	67

A.1. Top: m_{et} distribution; bottom: $m_{\mu t}$ distribution. Left: no other leptons present, right: additional lepton present. If a third lepton is present, its flavor is opposite of the first lepton, and its charge is the same as the track's (rejecting third leptons from Z). Note: This is from the dilepton-triggered dataset, i.e. the tracks used here probably were good enough leptons to trigger.	70
B.1. Overview of the object collections used in EventAnalyzer.	72

Chapter 1

Introduction

The Standard Model of particle physics (SM) [3, 4, 5] has been a grand success in describing the fundamental properties and interactions of elementary particles. Since its development in the second half of the 20th century, it has helped understand the basic principles of both how matter is formed on the microscopic level, and of how the universe—eventually a big agglomeration of interacting particles—behaves on the macroscopic scale as a consequence of the microscopic interactions.

While designed to describe experimental observations, the SM reaches beyond the mere reproduction experimental results. Its mathematical structure leads to predictions of what should be observed in experiments that have never been performed before. To verify the validity of such predictions and thus of the concepts of the SM itself, the scientific community has built massive accelerator machines such as the Large Hadron Collider (LHC) [6] which pushes charged particles to very high energies in order to have them collide at a defined point of interaction, around which detectors record the scatter particles with meticulous precision. This way, almost all SM predictions that have been put to an experimental test have been confirmed with extraordinarily high precision [7].

Nonetheless, some observations are inconsistent with SM assumptions. In particular, the discovery of neutrino oscillations shows that neutrinos are massive [8], which hints at physics beyond the Standard Model. However, an extension to the SM—the seesaw mechanism—aims to account for both the neutrino masses and their smallness (six or more orders of magnitude smaller than that of the electron) through the addition of new heavy particles coupling both to leptons and to Higgs doublets.

In this thesis, we pursue a broad search for the type-III seesaw signal [9] by examining the final state with at least three isolated prompt leptons (e, μ) using proton–proton collision data collected by the CMS detector [10] at the LHC in 2015.¹

The most notable backgrounds are WZ decaying to three leptons, fully leptonic $t\bar{t}$ decays with a fake² lepton from a b-jet, leptonic Z decays accompanied by a fake lepton, and leptonic ZZ decays. In addition to these, there are rare backgrounds such as $t\bar{t}Z$, $t\bar{t}W$, triboson, and Higgs production. The VV backgrounds ($V = W, Z$) are generally well modeled by Monte Carlo (MC) simulation. Backgrounds with fake leptons, however, are not as easily estimated by simulation and are thus derived from data. The background estimation methods employed in this search are enhanced versions of similar methods that have been used extensively in various CMS Run-I publications, e. g. [11, 12, 13, 14].

Prior results for this model include an 8 TeV CMS result [15] which sets exclusion limits for the flavor-democratic scenario at $m_\Sigma = 250$ GeV (expected) and $m_\Sigma = 278$ GeV (observed) based on trilepton channels, and an 8 TeV ATLAS result in the $\ell\ell jj$ final state [16] which extends to higher mass values, but cannot be directly compared because of different choices of mixing parameters and other model constraints. Both these results use datasets with an integrated luminosity of 20 fb^{-1} , whereas an older CMS result uses a 7 TeV dataset with 4.9 fb^{-1} [17].

Going from 8 TeV to 13 TeV, the signal cross section has increased by a factor of 3 for masses at the sensitivity limit between 300 and 400 GeV. Still, due to various analysis improvements which include new decay modes involving the Higgs boson, signal regions featuring an opposite-sign same-flavor pair consistent with a Z boson decay, 4-lepton channels, new kinematic variables, and refined background methods, the sensitivity with the current 2.3 fb^{-1} dataset at 13 TeV exceeds that of the Run I analysis.

¹This analysis has been announced publicly by CERN. A summary is thus also available as a Physics Analysis Summary (PAS) [2] on the CERN document server. The thesis author is also the PAS author.

²The term “fake” refers both to real leptons that arise from non-prompt decays, for instance: of hadrons, and to non-leptonic objects that are reconstructed as leptons. It is intended to denote all leptons that arise neither from bosonic decays nor from the signal.

Before describing the details of the analysis, an overview of the Standard Model and its shortcomings will be presented, accompanied by a description of the phenomenology of the type-III seesaw model which is suitable to solve some of these issues (Chapter 2). A brief description of the structure and the most important features of both the LHC accelerator and the CMS detector that was used to collect the data for this search follows (Chapter 3). After these rather generic sections, Chapters 4–9 continue to describe the analysis itself as well as the results.

Chapter 2

Theoretical Overview

2.1 Standard Model

The Standard Model (SM) is a relativistic quantum field theory describing all known fundamental interactions between elementary particles with the exception of gravity, i. e. it describes electromagnetism as well as the weak and strong interactions. One has not yet succeeded integrating gravity into the same framework. However, since gravitational effects are negligible LHC energies, gravity can be safely ignored for our purposes.

The SM makes use of several types of fields, each describing a different kind of particle. The model contains half-integer and integer spin particles (in units of the reduced Planck constant \hbar) which are called fermions and bosons, respectively. Refs. [3, 4] elaborate on the individual types of particles in greater detail.¹

2.1.1 Fermions

The fermion group² consists of two subgroups named leptons and quarks; both of them are subdivided into three so-called “generations”, or “flavors”.

¹The present section as well as Sec. 2.2 are largely taken from Ref. [1] (the author’s Master’s Thesis).

²“Group” is not meant in the mathematical sense here.

	particle	mass [MeV/c ²]	spin	electrical charge [e]
fermions				
leptons $L = 1,$ $B = 0$	e	0.511	1/2	-1
	ν_e	$0 < m_{\nu_e} < 2.2 \cdot 10^{-6}$	1/2	0
	μ	105.7	1/2	-1
	ν_μ	$0 < m_{\nu_\mu} < 0.17$	1/2	0
	τ	$1.78 \cdot 10^3$	1/2	-1
	ν_τ	$0 < m_{\nu_\tau} < 15.5 \cdot 10^{-6}$	1/2	0
quarks $L = 0,$ $B = 1/3$	u	2.4	1/2	2/3
	d	4.8	1/2	-1/3
	c	$1.27 \cdot 10^3$	1/2	2/3
	s	104	1/2	-1/3
	t	$173.34 \cdot 10^3$	1/2	2/3
	b	$4.2 \cdot 10^3$	1/2	-1/3
bosons				
$L = 0,$ $B = 0$	γ	0	1	0
	g	0	1	0
	Z	$91.2 \cdot 10^3$	1	0
	W^\pm	$80.4 \cdot 10^3$	1	± 1
	H	$125.09 \cdot 10^3$	0	0

Table 2.1: Elementary particles in the Standard Model [7, 18, 19]. For electrically charged particles, anti-particles with opposite charge exist. Neutrinos presumably have anti-particles with opposite chirality. Anti-particles have been omitted in this summary.

Leptons

The three lepton generations are

$$\begin{pmatrix} \nu_e \\ e \end{pmatrix}, \quad \begin{pmatrix} \nu_\mu \\ \mu \end{pmatrix}, \quad \begin{pmatrix} \nu_\tau \\ \tau \end{pmatrix}, \quad (2.1)$$

where e, μ, τ are similar particles of electrical charge -1 and spin $1/2$. However, their masses are quite different (see Table 2.1). In interactions, they usually appear with the corresponding neutrino ν_ℓ , $\ell = e, \mu, \tau$.

In addition to these six particles, there are also six antiparticles with opposite charge sign and lepton number.³ The present analysis is concerned with events exhibiting three or more electrons or muons.

Quarks

There are six quarks called up, down, charm, strange, top, and bottom quark. They are organized in generations as follows:

$$\begin{pmatrix} u \\ d \end{pmatrix}, \quad \begin{pmatrix} c \\ s \end{pmatrix}, \quad \begin{pmatrix} t \\ b \end{pmatrix}, \quad (2.2)$$

where the particles in the upper row are of electrical charge $+2/3$, and those in the lower row have electrical charge $-1/3$. Anti-quarks have opposite charge and baryon number. As quarks are subject to strong interaction, they carry an additional “color” charge which is either “red”, “green”, or “blue”.

Quarks have not been observed individually. In the SM, they thus form bound states such that the electrical charge is integer and the color charge vanishes or adds up to “white” (i. e. all three colors are present). Particles consisting of three quarks are called baryons

³It is also possible that neutrinos are Majorana fermions and thus their own anti-particles, as is the case in the type-III seesaw model, for example. This question has not yet been answered experimentally.

(for example the proton: $p \cong uud +$ valence quarks), and quark–antiquark combinations are called mesons (for example the pion: $\pi^+ \cong u\bar{d}$).

2.1.2 Bosons

The quantum field theory on which the SM is built is invariant under Lorentz and CPT transformations, and under certain gauge transformations. To prevent the theory from losing this invariance, the existence of so-called gauge bosons was predicted, and indeed later observed. These particles act as the force carriers of the fundamental forces.

The most well-known one is the massless photon (γ) which is electrically neutral and mediates the electromagnetic interaction. A very similar particle, although massive, is the Z boson which can interact electromagnetically and weakly. Furthermore, the charged W^+ and W^- bosons exist. Conceptually, they have the same origin as the Z boson, which is why they take part in the same interactions.⁴ A great theoretical achievement was the unification of the electromagnetic and the weak interaction into a combined concept, the electroweak interaction.

The strong force between quarks is carried by the massless gluons (g) which come in eight different color-anticolor combinations.

2.2 Shortcomings of the Standard Model

While the Standard Model predicts the electromagnetic, weak, and strong phenomena with extraordinary precision, there are open questions that are not addressed by the SM:

- The Standard Model does not account for *gravity* at all. It is described by General Relativity, and it is believed that, in principle, a unification of the theories is possible.
- The Standard Model does not explain *Dark Matter* [20].

⁴In fact, the γ and Z fields are superpositions of the more fundamental B and W^0 fields. The B field arises from spontaneous $U(1)$ symmetry breaking, while the W^i come from the breaking of $SU(2)$.

- The Standard Model contains a number of parameters that differ from expectation by several orders of magnitude for unknown reasons. For example, the mass of the Higgs boson was expected to be around 10^{15} GeV due to top quark loops, but it is in fact on the electroweak scale [19]. This issue is referred to as the *Hierarchy Problem* [21].
- The Standard Model assumes the neutrinos to be massless. However, the existence of oscillations between neutrino flavors has been experimentally observed, implying that their mass is in fact non-zero [22, 23, 8].

While the first two issues represent aspects of Nature that lie outside the scope of the SM, it does describe neutrinos and the Higgs boson. However, any motivation for the observed values remains unclear; the mass puzzles are therefore rather delicate.

Several attempts have been made to find remedies for these issues from a theoretical point of view, and because they come with predictions of new particles, they are subject to experimental examination. The seesaw mechanism aims to provide answers to the question of how neutrinos acquire mass.

2.3 Type-III Seesaw Mechanism

2.3.1 Phenomenology

The seesaw mechanism introduces new heavy particles coupling both to leptons and to Higgs doublets, and accounts for both the neutrino masses and their smallness (six or more orders of magnitude smaller than that of the electron) [24, 25, 26, 27, 28, 29, 30, 31, 32, 9, 33].

Within the type-III seesaw model [9], the neutrino is considered a Majorana particle whose mass arises via the mediation of massive fermion partners. These massive partners are the fermionic $SU(2)$ triplet of the heavy Dirac charged leptons Σ^\pm , and the heavy Majorana neutral lepton Σ^0 , coupling both to the leptons and to the Higgs doublets. During proton-proton collisions, the heavy fermion particles may be pair-produced through electroweak interactions in both charged-charged and charged-neutral pairs as can be seen in Fig. 2.1.

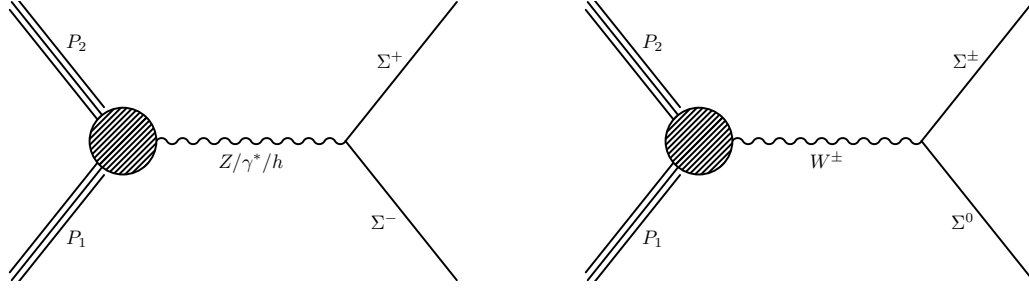


Figure 2.1: Examples of Feynman diagrams for heavy fermion production in the type-III seesaw model.

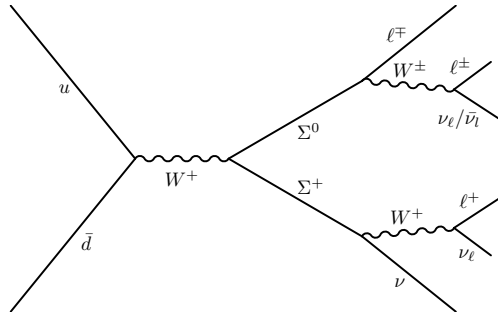


Figure 2.2: Feynman diagram example of the fermion production and decay in the type-III seesaw model.

We conduct a search for this signal by examining the final state with at least three electrons or muons. The primary decay channels of interest are $\Sigma^\pm \rightarrow W^\pm \nu$, $\Sigma^\pm \rightarrow Z \ell^\mp$, $\Sigma^\pm \rightarrow H \ell^\pm$, $\Sigma^0 \rightarrow W^\pm \ell^\mp$, $\Sigma^0 \rightarrow Z \nu$, $\Sigma^0 \rightarrow H \nu$, where $\ell = e, \mu$. Decays of $\Sigma^0 \Sigma^\pm$ and $\Sigma^+ \Sigma^-$ pairs result in 27 different production processes and can naturally lead to multilepton final states if several W or Z bosons are involved, either directly or via a Higgs boson decay. An example Feynman diagram for one of the most relevant processes with three leptons in the final state, $\Sigma^\pm \Sigma^0 \rightarrow W^\pm \nu W^\pm \ell^\mp$ with leptonic W^\pm decays, is shown in Fig. 2.2. The decay rate of a Σ to a given lepton ℓ is proportional to $v_{\ell N} = \frac{V_\ell}{\sqrt{|V_e|^2 + |V_\mu|^2 + |V_\tau|^2}}$. In the democratic scenario, the mixing parameters V_ℓ are the same for all the leptons so that $v_{\ell N} = \frac{1}{\sqrt{3}}$.

2.3.2 Signal Model and Generation

We generate MC events to simulate all 27 production and decay mode combinations (see Sec. 1). Generation for the model begins with a FeynRules Model file [34]. SaloMonte Carlo

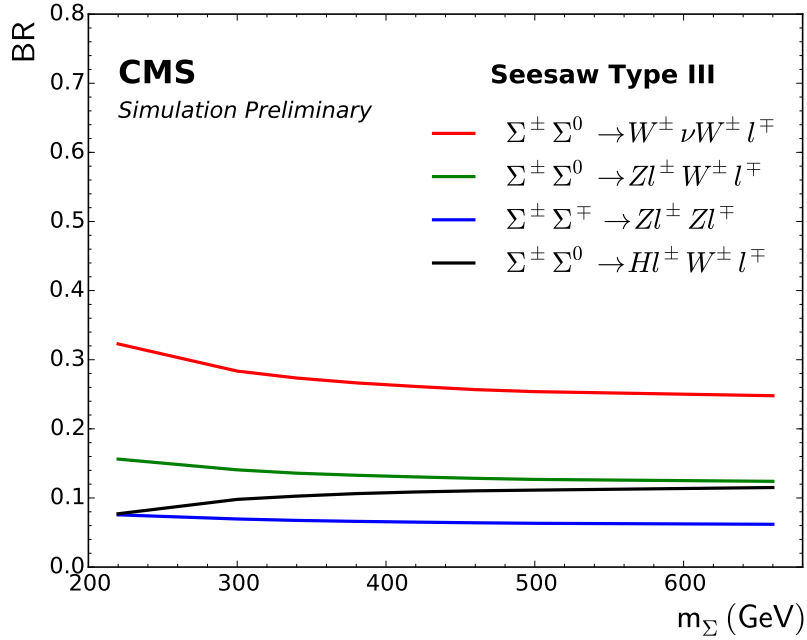


Figure 2.3: Branching ratios from the pair-produced fermions to the bosonic level of the most relevant decay modes.

events are then generated in MadGraph5_aMC@NLO [35]. Bosonic decays are handled through Pythia 8, which is also in charge of hadronization [36]. At the analysis level, we apply weights to correct for mismodeling of pile-up and E_T^{miss} resolution.

The production cross sections were calculated with NLO + NLL accuracy using the CTEQ6.6 and MSTW2008nlo90cl parton distribution functions (PDFs) [37, 38]. Flavor-democratic values of the mixing angles are taken ($V_e = V_\mu = V_\tau = 10^{-6}$). This has no direct consequence on the fermion production cross section, but affects the branching ratios. The branching fraction of a heavy fermion to a lepton of flavor $\ell = e, \mu, \tau$ is proportional to $v_{\ell N} = \frac{V_\ell}{\sqrt{|V_e|^2 + |V_\mu|^2 + |V_\tau|^2}}$. The branching ratios from the pair-produced fermions to the bosonic level of the most relevant decay modes are given in Fig. 2.3.

Chapter 3

Experimental Apparatus¹

3.1 The Large Hadron Collider

The particle collisions analyzed in the present thesis were generated by the Large Hadron Collider (LHC) which is located 100 m underground in the French–Swiss border area at the outskirts of Geneva [39]. Several pre-accelerators are employed in order to accelerate the protons to different energies and to split them into bunches, before they reach the LHC ring (see Fig. 3.1) to form two beams traveling in opposite directions. In this ring of 26.7 km circumference, 1232 superconducting dipole magnets are used to produce a magnetic field of up to 8.33 T in order to accelerate the protons to their final center of mass energy of $\sqrt{s} = 13 \text{ TeV}$. Additionally, about 7000 magnets are used for trajectory corrections and bunch focusing. Once the final velocity is reached, the protons are directed onto each other at certain points around the accelerator ring, where they collide. The collision products, in general, are not stable, but decay to intermediate and final state particles which are detected by large detector devices such as ATLAS or CMS. The bunch spacing is such that interactions are separated in time by 25 ns.²

The design luminosity of LHC is $10^{34} \text{ cm}^{-2}\text{s}^{-1}$. The instantaneous luminosity is given by

$$L = \frac{N_p^2 n_b f_{\text{rev}} \gamma_r}{4\pi \epsilon_n \beta_*} F \quad (3.1)$$

¹This chapter is largely taken from Ref. [1] (the author’s Master’s Thesis).

²However, several interactions might occur at the same time when two bunches meet. This phenomenon is referred to as “pile-up” and must be corrected for at analysis time, mostly by means of geometrical separation of the primary interaction vertex and by subtraction of expected pile-up contributions.

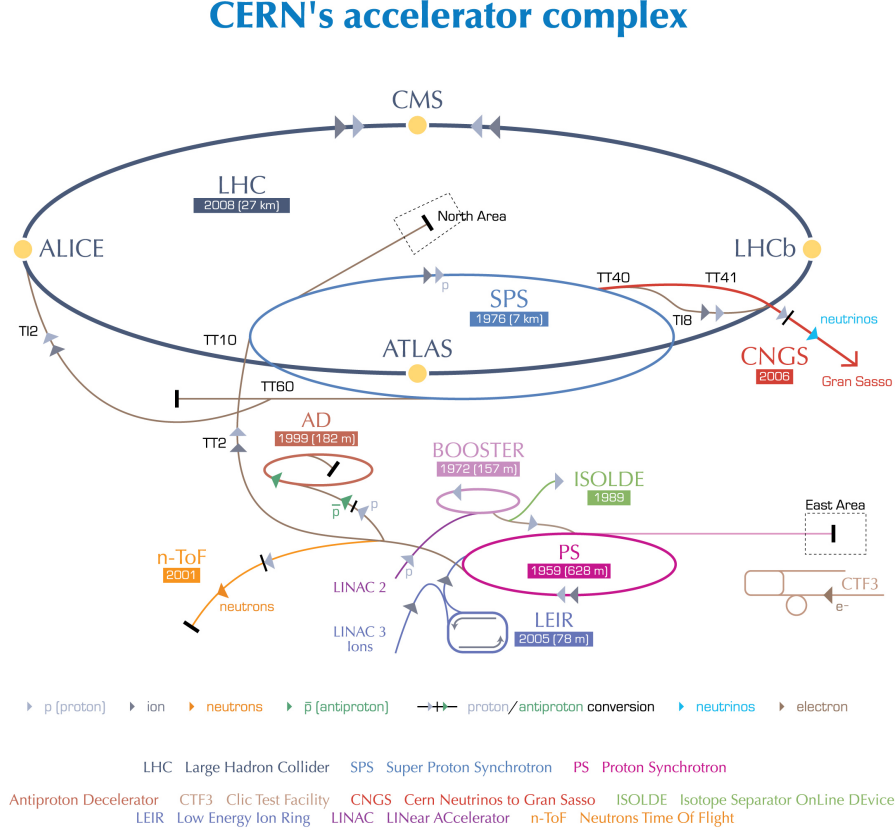


Figure 3.1: CERN Accelerator Complex [40]. The diagram shows the different accelerators, detectors, and other facilities at CERN. For proton collisions, not all of the machinery is needed: Protons are initially accelerated to 50 MeV in a Linear Accelerator (LINAC 2). Then, they are transported to the Booster (1.4 GeV), to the Proton Synchrotron (PS, 25 GeV) and the Super Proton Synchrotron (SPS, 450 GeV) from where they are injected into LHC. The PS also takes care of arranging the protons in bunches with the correct spacing for LHC.

where N_b is the number of particles per bunch, n_b is the number of bunches per beam, f_{rev} is the revolution frequency, γ_r is the relativistic gamma factor, ϵ_n is the normalized transverse beam emittance, β^* is the beta function at the collision point, and F is the geometric luminosity reduction factor due to the crossing angle at the interaction point.

3.2 The CMS Detector

The Compact Muon Solenoid (CMS) is located at point 5 of the LHC accelerator ring and one of the two large, general purpose detector systems built at LHC. CMS consists of a large superconducting solenoid which contains a silicon-based tracker, an electromagnetic

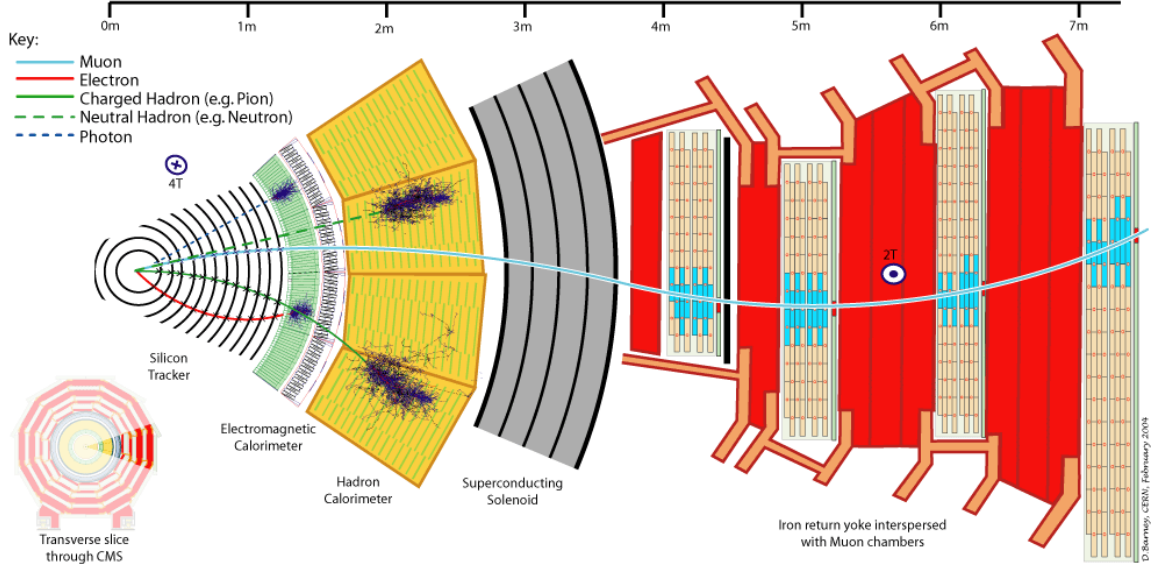


Figure 3.2: A transverse slice through CMS [41]. The illustration shows the most important detector components as well as examples of different particles as they are detected while traveling through the detector.

calorimeter made of scintillating lead-tungstate crystals, and a brass-based scintillating hadron calorimeter (see Fig. 3.2); the total weight is about 12500 tons [10]. A special feature of CMS is its superconducting solenoid of 6 m internal diameter which creates a strong magnetic field (3.8 T) that is suitable for high precision measurements of charged particles at very high energies.

In order to describe the properties of particles observed in collision events, a coordinate system is defined. The origin is declared where the main interaction point is expected to occur. The x axis points radially towards the center of the LHC, the y axis points in the upward direction, and together with the z axis that points along the beampipe (counterclockwise), a right-handed coordinate system is constructed. In cylindrical coordinates, the z axis is the same, and ϕ is the azimuthal angle. Starting from the positive z axis, the polar angle θ increases towards the center of the LHC. Since the polar angle θ is not Lorentz-invariant,

the pseudorapidity η is defined as a Lorentz-invariant alternative coordinate,³

$$\eta = -\log \tan \frac{\theta}{2}. \quad (3.2)$$

When the directional separation between particles needs to be determined,

$$\Delta R = \sqrt{(\Delta\eta)^2 + (\Delta\phi)^2} \quad (3.3)$$

comes in handy as a measure of two particles' separation in η and ϕ .

The following sections are concerned with the individual detector components used for the measurement of the particle properties that are recorded from collision events, along the lines of Ref. [42].

3.2.1 Tracking System

In order to precisely reconstruct the path of charged particles in CMS, a tracking system based on silicon-based p–n junctions was installed. A high reverse-bias voltage is applied across the junction, creating a depletion zone with an electric field. When a charged particle passes this zone, it ionizes the silicon atoms, and the resulting electrons are free to move and create an electrical current which is detected. By setting up several layers containing a large number of such p–n junctions with small dimensions, a highly sensitive tracking device can be created. In total, 15400 tracking sensors are installed in CMS and operated at low temperature in order to minimize the effects of radiation damage. The CMS tracking system consists of several parts:

³This quantity is the massless limit of the rapidity which is an additive measure of relativistic velocity and defined as $\log \frac{E+p_z}{E-p_z}$.

Pixel Detector

The Pixel Detector is located within 10 cm from the z axis and is used to account for small displacements close to the primary vertex. To keep the occupancy per bunch crossing reasonably low, a pixel size of $100 \mu\text{m} \times 150 \mu\text{m}$ is used. The spatial resolution is $10 \mu\text{m}$ to $20 \mu\text{m}$.

Strip Detector

The Strip Detectors are located both in the barrel as well as in the endcap regions of CMS. In either case, several layers of silicon strips are placed behind each other to provide similar functionality as in the case of the pixel detector. The dimensions are much wider than those of the pixels. In each detector region, they are chosen according to the corresponding production characteristics such that the occupancy will not be too high, so that a hit will provide informative value.

3.2.2 Electromagnetic and Hadronic Calorimeter

The calorimetry system is designed to measure the energies of incident particles. Depending on the particle type, the energy is deposited in different parts of the system [43]:

Electromagnetic Calorimeter (ECAL)

The task of the ECAL is to measure the energy of charged particles (especially electrons) and photons. The lead-tungstate (PbWO_4) material of the crystals is very dense, but optically transparent; a module is shown in Fig. 3.3. When electrons or photons travel through, they lose energy in a cascade process due to bremsstrahlung and ionization (electrons) and e^+e^- pair production (photons). In addition, the crystals are excited so that they produce light from scintillation which is detected by photodetectors and used to infer the incident particle's energy.



Figure 3.3: A module of the electromagnetic calorimeter consisting of 500 lead-tungstate crystals.

In the barrel ($|\eta| \leq 1.479$), there are 61200 crystals with front face dimensions of $22\text{ mm} \times 22\text{ mm}$, covering 0.0174 in both η and ϕ , and a length of 230 mm, corresponding to about 25 radiation lengths. In the endcap ($1.479 \leq |\eta| \leq 3.0$), there are 7324 crystals with a surface area of $28.6\text{ mm} \times 28.6\text{ mm}$ and a length of 220 mm. An additional preshower detector is installed in front of the endcap component that helps distinguishing photons from neutral pions. This setup covers the η range up to the forward region without any gaps.

Hadronic Calorimeter (HCAL)

Like the ECAL, the HCAL is for the most part located inside the solenoid. While the ECAL is a homogeneous, the HCAL is a sampling calorimeter which means that it consists of alternating layers of an active, signal-generating medium, and a passive medium whose only purpose is to absorb energy. The active material is a plastic scintillator which is 3.7 mm thick and organized in a tile pattern. The scintillation light emitted in a certain η - ϕ cell is summed up optically, forming a “tower”, collected by wavelength-shifting fibers, and channeled to hybrid photodiodes.

The barrel part ($|\eta| \leq 1.4$) has 2304 towers, each covering 0.087 in η and ϕ . There are 15 absorption layers, mostly made from brass. To increase accuracy, a number of layers is placed at the outside of the magnet coil (Hadron Outer, HO). The endcap parts cover the region $1.3 \leq |\eta| \leq 3.0$ with 19 layers of active scintillating material, covering cell of width 5° to 10° in ϕ and 0.35 to 0.09 in η . In the very forward region ($3.0 \leq |\eta| \leq 5.0$), a fourth HCAL part (Hadron Forward, HF) consisting of an active quartz fiber medium and steel absorbers is located. The quartz fiber material emits Čerenkov light that is detected by photomultipliers with resolution 0.175 in η and 10° in ϕ .

3.2.3 Muon System

The muon is about 200 times as heavy as the electron. Since the bremsstrahlung-induced dissipation in the calorimeter is proportional to mass $^{-2}$ [44], it is suppressed by a factor of 40000. Therefore, muons can easily traverse the calorimeter system, so that other more specialized detector systems can be employed outside the calorimeter.

In the barrel, 250 drift tube (DT) chambers are used to identify muons. Four shells of stations are located at different distances from the z axis, embedded in the return yoke of the solenoid (see Fig. 3.4). In the endcap, 468 cathode strip chambers (CSC) are arranged in concentric rings, most of them containing 36 CSCs. Charged particles travelling through the gas inside a CSC cause ionization, followed by a charged avalanche whose distribution is measured on the cathode plane. From this information, it is possible to reconstruct the track geometry. Each of the DT and CSC stations is accompanied by resistive plate chambers that are used for precise timing and velocity determination.

3.2.4 Trigger and Data Storage

LHC performs about about 10^7 – 10^8 proton–proton collisions per second. Since not all events can be stored (about 300 Hz), a rejection rate of about 10^5 is required. First-level decisions are reached by the Level-1 (L1) trigger system which performs quick assessments of events

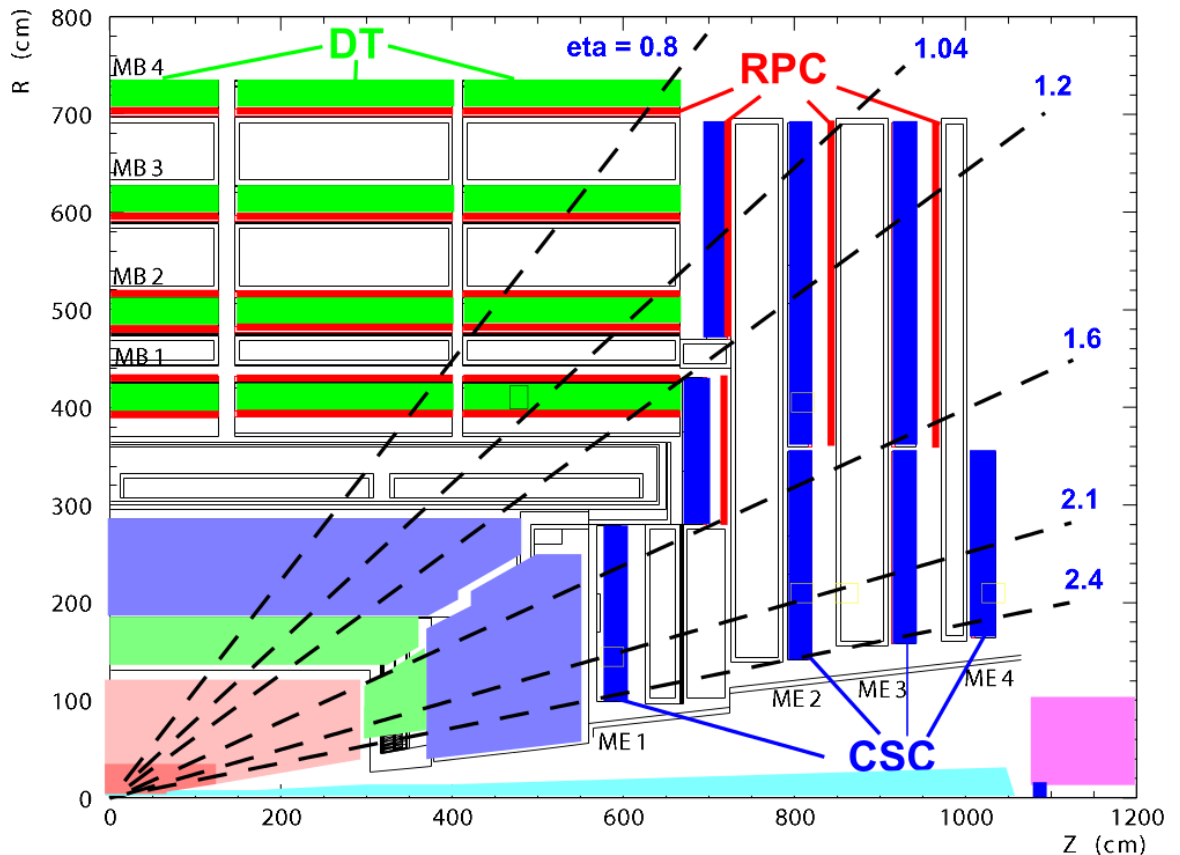


Figure 3.4: Sketch of the muon system in CMS in r - z view. The drift tubes are displayed in dark-green, the cathode strip chambers in dark-blue, and the resistive plate chambers in dark-red. The light-colored areas are the tracker and calorimeter. The interaction point is located at the origin of the coordinate system.

within about $1\ \mu\text{s}$ while the event data, about 0.5 MB each, is held in buffers. Potentially interesting events are then forwarded to a dedicated computing farm where high-level triggers (HLT) run more precise reconstruction algorithms in order to decide which events should be kept.

Finally, accepted events are transmitted to the storage manager system which arranges the subsequent transfer to the permanent Tier-0 storage systems located at the CERN main site and at the Wigner Research Centre for Physics in Budapest (Hungary). From there, data is distributed to interested Tier-1 and Tier-2 sites across the globe for analysis purposes. Petabyte-range storage systems are employed world-wide to manage the large amounts of data that are used on a daily basis.

Chapter 4

Datasets and Triggers

4.1 Triggers

The data for this search are collected using several dilepton triggers. The double electron trigger requires two electrons with p_T thresholds of 17 GeV on the leading electron and 12 GeV on the sub-leading electron. The double muon trigger requires two muons with p_T thresholds of 17 and 8 GeV on the leading and sub-leading muons, respectively. We use two muon/electron cross triggers, one of which requires a 17 GeV muon and a 12 GeV electron, while the other requires a 17 GeV electron and a 8 GeV muon.

We use the data sets listed in Table 4.1, masked using the “Golden JSON file” `/afs/cern.ch/cms/CAF/CMSCOMM/COMM_DQM/certification/Collisions15/13TeV/Reprocessing/Cert_13TeV_16Dec2015ReReco_Collisions15_25ns_JSON_v2.txt`.

4.2 Background MC samples

For background determination, we use the Monte Carlo samples listed in Table 4.2.

Some MC generators provide events with negative weights to allow for a more precise

Table 4.1: Data samples.

Primary Dataset	Reconstruction labels	$L [fb^{-1}]$
DoubleEG	Run2015D-05Oct2015-v1	0.59
DoubleEG	Run2015D-PromptReco-v4	1.66
DoubleMuon	Run2015D-05Oct2015-v1	0.59
DoubleMuon	Run2015D-PromptReco-v4	1.66
MuonEG	Run2015D-05Oct2015-v1	0.59
MuonEG	Run2015D-PromptReco-v4	1.66

Table 4.2: Background MC samples.

Sample	xsec [pb]	L [pb^{-1}]	No. events read
/WZTo3LNu_TuneCUETP8M1_13TeV-powheg-pythia8	4.42965	447169	1.9808e+06
/RunIISpring15DR74-Asympt25ns_MCRUN2_74_V9-v1/MINIAODSIM			
/WZJets_TuneCUETP8M1_13TeV-amcatnloFXFX-pythia8/	5.263	2.37929e+06	1.252220e+07
RunIISpring15MiniAODv2-74X_mcRun2_asymptotic_v2-v1/MINIAODSIM			
/ZZTo4L_13TeV-amcatnloFXFX-pythia8	1.212	8.71378e+06	1.05611e+07
/RunIISpring15DR74-Asympt25nsRaw_MCRUN2_74_V9-v1/MINIAODSIM			
/TTTo2L2Nu_13TeV-powheg	87.31	69711.1	4.997e+06
/RunIISpring15DR74-Asympt25ns_MCRUN2_74_V9-v1/MINIAODSIM			
/TTWJetsToLNu_TuneCUETP8M1_13TeV-amcatnloFXFX-madspin-pythia8	0.2043	1.23792e+06	252908
/RunIISpring15DR74-Asympt25ns_MCRUN2_74_V9-v1/MINIAODSIM			
/TTZToLLNuNu_M-10_TuneCUETP8M1_13TeV-amcatnlo-pythia8	0.2529	1.57374e+06	398000
/RunIISpring15DR74-Asympt25ns_MCRUN2_74_V9-v1/MINIAODSIM			
/WWZ_TuneCUETP8M1_13TeV-amcatnlo-pythia8/	0.1651	1.51423e+06	250000
RunIISpring15MiniAODv2-74X_mcRun2_asymptotic_v2-v1/MINIAODSIM			
/WZZ_TuneCUETP8M1_13TeV-amcatnlo-pythia8/	0.05565	4.49236e+06	250000
RunIISpring15MiniAODv2-74X_mcRun2_asymptotic_v2-v1/MINIAODSIM			
/ZZZ_TuneCUETP8M1_13TeV-amcatnlo-pythia8/	0.01398	1.78827e+07	250000
RunIISpring15MiniAODv2-74X_mcRun2_asymptotic_v2-v1/MINIAODSIM			
/GluGluHToZZTo4L_M125_13TeV_powheg_JHUGen_pythia8	0.01212	4.10891e+07	498000
/RunIISpring15MiniAODv2-74X_mcRun2_asymptotic_v2-v1/MINIAODSIM			
/VBF_HToZZTo4L_M125_13TeV_powheg_JHUGen_pythia8	0.001034	4.73362e+08	489456
/RunIISpring15MiniAODv2-74X_mcRun2_asymptotic_v2-v1/MINIAODSIM			
/DYJetsToLL_M-10to50_TuneCUETP8M1_13TeV-amcatnloFXFX-pythia8	18610	1613.2	3.002156e+07
/RunIISpring15MiniAODv2-74X_mcRun2_asymptotic_v2-v1/MINIAODSIM			
/DYJetsToLL_M-50_TuneCUETP8M1_13TeV-amcatnloFXFX-pythia8	6025.2	4771.29	2.874797e+07
/RunIISpring15MiniAODv2-74X_mcRun2_asymptotic_v2-v1/MINIAODSIM			

prediction of higher-order contributions. Where provided, we take these negative weights into account.

For each MC sample, the pile-up distribution is compared to the distribution in data. Weights are applied on a per-event basis so that the distribution matches for each sample.

We also correct the pile-up dependence of our data-driven background estimate using the linear fit $0.773 + 0.0218 \cdot n_{\text{vertex}}$. As a result of these weights, the background shape of the n_{vertex} distribution agrees with the data. Fig. 4.1 shows this distribution before and after pile-up weights for events with at least three electrons or muons, without any other cuts.

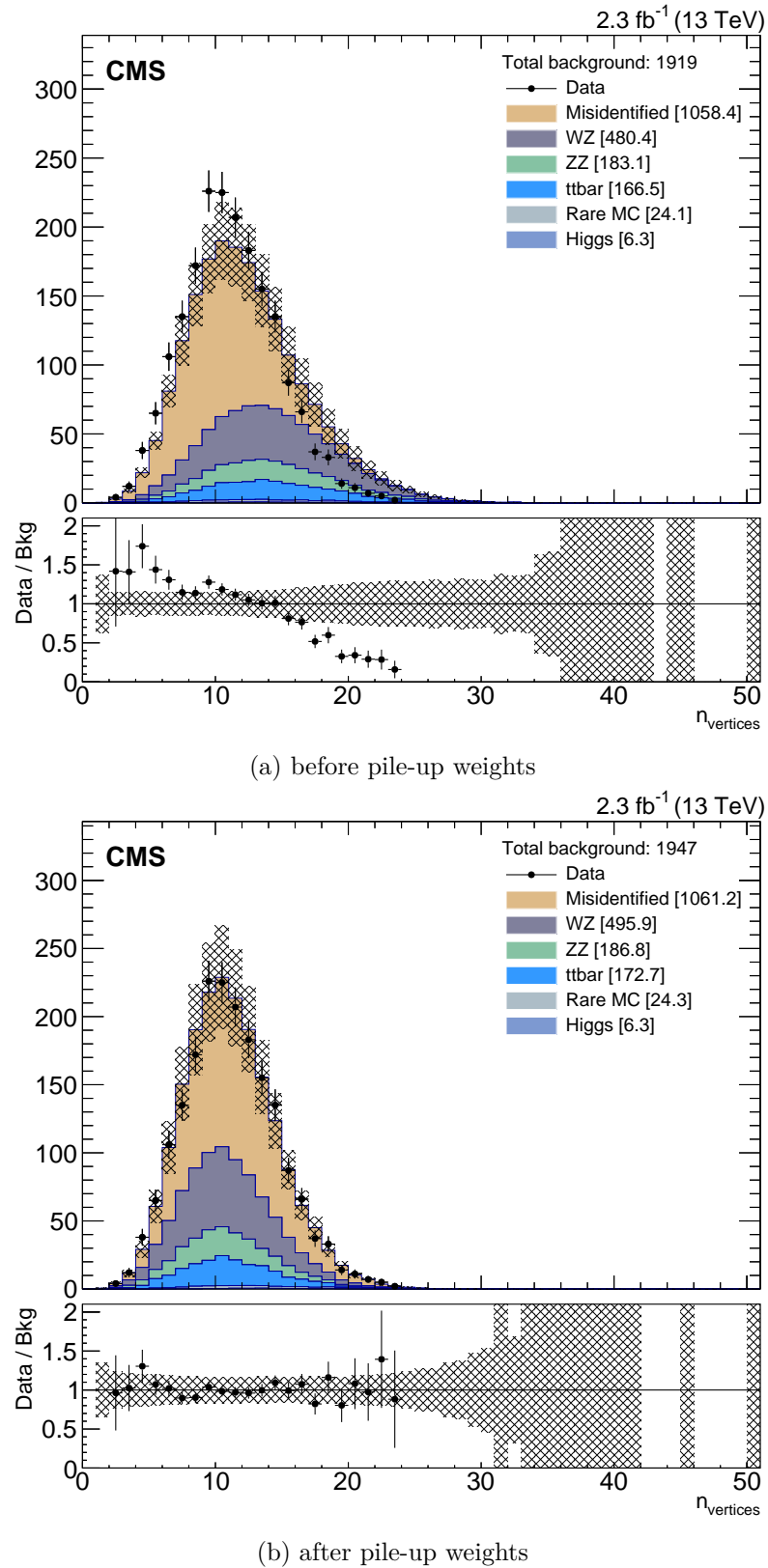


Figure 4.1: n_{vertex} distribution for events with at least three light leptons.

Chapter 5

Selection

5.1 Object Selection

5.1.1 Electrons and Muons

Events that pass the trigger are required to satisfy additional selection criteria. Electrons with $p_T \geq 7 \text{ GeV}$ and $|\eta| \leq 2.5$ as well as muons with $p_T \geq 5 \text{ GeV}$ and $|\eta| \leq 2.4$ are reconstructed using the particle-flow (PF) algorithm which utilizes measured quantities from the tracker, calorimeter, and muon system [45]. The matching candidate tracks must satisfy quality requirements and spatially match with the energy deposits in the ECAL and the tracks in the muon detectors, as appropriate.

Sources of background leptons include genuine leptons occurring inside or near jets, hadrons that punch through into the muon system and are misidentified as muons, hadronic showers with large electromagnetic fractions, or photon conversions. Since the leptons from the seesaw signal are generally not related to hadronic activity, electrons and muons are expected to be spatially isolated from any jets occurring in the event. As jets occasionally produce leptons in their vicinity, an isolation requirement strongly reduces the background from such fake leptons.

The isolation requirement imposes a selection based on the size of the lepton transverse momentum in comparison to the transverse momenta of other particles in its immediate neighborhood. A customary isolation discriminator is the “relative isolation”,

$$I_{\text{rel}}(\Delta R^{\max}) = \frac{\sum_{\text{other}}^{\Delta R < \Delta R^{\max}} p_T^{\text{other}}}{p_T^\ell}, \quad (5.1)$$

defined as the transverse momentum sum of charged hadrons, neutral hadrons, and photons within a ΔR^{\max} cone around the lepton candidate, divided by the lepton's own p_T .

However, as the masses of the heavy fermions in the seesaw model are high, their decay products are expected to be boosted and thus harder to distinguish geometrically. The relative isolation variable therefore does not provide good enough separation. We therefore use the multi-isolation discriminator which has better discrimination power in the case of boosted topologies [46]. This is achieved using the following three input variables:

1. A modified version of the relative isolation I_{rel} , called mini-isolation (I_{mini}) [47]. Just like I_{rel} , it is the ratio of the scalar sum of the transverse momenta of charged hadrons, neutral hadrons, and photons within a cone around the lepton candidate; however, the cone radius depends on the transverse momentum of the lepton candidate itself:

$$\Delta R^{\max}(p_T^\ell) = \frac{10 \text{ GeV}}{\min [\max(p_T^\ell, 50 \text{ GeV}), 200 \text{ GeV}]} . \quad (5.2)$$

The cone size thus varies from 0.2 to 0.05 as a function of the lepton p_T and is smaller for higher values of the lepton p_T , reducing the chance of overlap with other objects as the lepton becomes stiffer. Besides, as fake leptons usually have rather low p_T , the larger cone size for low- p_T leptons improves the background rejection efficiency.

2. We use the ratio of the lepton p_T and the p_T of the jet in which the lepton is contained,

$$p_T^{\text{ratio}} = \frac{p_T^\ell}{p_T^{\text{jet}}} . \quad (5.3)$$

Note that every lepton is, by definition, contained in a jet (which may contain nothing else besides the lepton). The p_T^{ratio} variable thus tells us the share of the jet momentum that is associated with the lepton. The larger this fraction, the lesser is the chance that the lepton stems from a hadronic decay or is misidentified. This variable is similar to I_{rel} , except that the cone is replaced by the jet.

Table 5.1: Multi-isolation working points used in the analysis.

Isolation value	Muons	Electrons
I_1	0.20	0.16
I_2	0.69	0.76
I_3 [GeV]	6.0	7.2

3. To avoid rejecting leptons that fail the p_T^{ratio} requirement because they overlap accidentally with another jet in the event, we consider the lepton candidate p_T along the axis of the residual momentum of the closest jet after subtracting the lepton p_T :

$$p_T^{\text{rel}} = \frac{(\vec{p}(\text{jet}) - \vec{p}(\ell)) \cdot \vec{p}(\ell)}{|\vec{p}(\text{jet}) - \vec{p}(\ell)|}. \quad (5.4)$$

If the p_T^{ratio} condition is not met while the lepton still has substantial momentum along the residual momentum axis, the lepton is allowed to pass.

A lepton is considered to be isolated if the following condition is met:

$$I_{\text{mini}} < I_1 \wedge (p_T^{\text{ratio}} > I_2 \vee p_T^{\text{rel}} > I_3) \quad (5.5)$$

The values of I_i , $i = 1, 2, 3$, depend on the lepton flavor. For electrons, the medium working point is employed, while for muons, we use the tight working point. As the chance of misidentification is higher for electrons, tighter isolation values are used in this case (see Table 5.1). Further details on the input variables, these and other working points, and their efficiencies can be found in [46].

The signal leptons originate from the interaction point. After the isolation selection, the most significant background sources are residual non-prompt leptons from heavy quark decays, where the lepton tends to be more isolated because of the high p_T with respect to the jet axis. This background is reduced by requiring that the leptons satisfy $d_z \leq 0.1$ cm where d_z is the longitudinal impact parameter with respect to the primary interaction vertex, and that the impact parameter d_{xy} between the track and the event vertex in the plane

transverse to the beam axis be small: $d_{xy} \leq 0.05$ cm. The isolation and impact parameter criteria retain signal but significantly reject fake leptons.

5.1.2 Missing Transverse Momentum (E_T^{miss})

The missing transverse momentum is calculated as the negative vectorial sum of the transverse momenta of all the PF candidates. The missing transverse energy E_T^{miss} is defined as the magnitude of this vector. Jet energy corrections are applied to all jets and also propagated to the calculation of E_T^{miss} [48]. We apply additional smearing to simulation samples to model the E_T^{miss} resolutions we find in data as a function of jet activity and the number of interaction vertices in an event.

5.2 Event Selection

For the three leading leptons, we apply offline thresholds of 20, 15, 10 GeV. We find that with these thresholds, the trigger efficiency of trilepton events is close to 100%.

Events with an opposite-sign lepton pair with mass below 12 GeV are vetoed to reduce background from low-mass resonances.

Chapter 6

Search Strategy

6.1 General Approach

Candidate events in this search must have a total of at least three leptons, each of which can be either an electron or a muon. We classify multilepton events into search channels on the basis of the number of leptons, lepton flavor, lepton relative charges, charge and flavor combinations, and other kinematic quantities described below.

We classify each event in terms of the maximum number of opposite-sign same-flavor (OSSF) dilepton pairs that can be made by using each lepton only once. For example, both $\mu^+\mu^-\mu^-$ and $\mu^+\mu^-e^-$ are OSSF1, $\mu^+\mu^+e^-$ is OSSF0, and $\mu^+\mu^-e^+e^-$ is OSSF2. We denote a lepton pair of different flavors as $\ell\ell'$.

We classify events as containing a leptonically-decaying Z if at least one OSSF pair has $m_{\ell^+\ell^-}$ in the Z mass window (91 ± 10) GeV. For $m_{\ell^+\ell^-}$ outside the Z boson mass window, events are separated into bins below and above the Z mass window. We refer to these three mass ranges as “on-Z”, “below-Z”, and “above-Z”.

In cases of ambiguity (such as $\mu^+\mu^-\mu^-$ with one pair below and one pair above Z), we need to pick a specific pair. We compare two methods:

1. Choose the pair whose invariant mass is closest to the Z mass.
2. Choose the pair closest to the Z mass, with the additional condition that pairs above the Z window are not considered if there is a pair below the Z window (thus shifting events from above-Z to below-Z).

Fig. 6.1 shows that there is little difference between both approaches. Nevertheless, we take the second approach to achieve a more separative categorization of background, especially around the high end of the Z window.

The most important multilepton background processes are WZ, ZZ production, and Z or $t\bar{t}$ events in which there is an additional fake lepton. The term “fake” refers both to real leptons that arise from non-prompt decays (for instance: of hadrons) and to non-leptonic objects that are reconstructed as leptons. It is intended to denote all objects reconstructed as leptons that arise neither from leptonic boson decays nor from the signal. At times, the term “misidentified” is used synonymously.

In addition to the aforementioned backgrounds, there are various rare processes like WWZ or $t\bar{t}W$. However, the level of SM background varies considerably across channels; for example, channels containing OSSF pairs suffer from larger backgrounds than do channels with OSSFO. Hence, all these charge combinations are considered as different channels.

6.2 Signal Regions

Backgrounds can be tamed by binning in appropriate quantities. Given the relatively high signal lepton momenta due to the large masses of the parent particles, cutting on L_T , the scalar lepton p_T sum, may be a good idea. This is especially true for decay modes like $\Sigma^\pm \rightarrow \ell^\pm Z \rightarrow \ell^\pm \ell'^\pm \ell'^\mp$ where the heavy fermion mass is transformed into the lepton momenta. However, such an L_T cut acts at the expense of the signal efficiency in other modes like $\Sigma^0 \rightarrow H\nu \rightarrow WW\nu$, where lepton p_T ’s are somewhat lower because the intermediate bosons may be off-shell, and the neutrinos carry away some of the momentum that appears as missing transverse energy (E_T^{miss}). However, we can still achieve high efficiency by using $L_T + E_T^{\text{miss}}$ instead, which we found suitable for signal selection for both of the described channel types (Fig. 6.2). The background rejection effectiveness of this variable is shown in Fig. 6.3. We find that lepton p_T binning alone gives about 20 % worse signal-to-background ratios in the most sensitive signal regions.

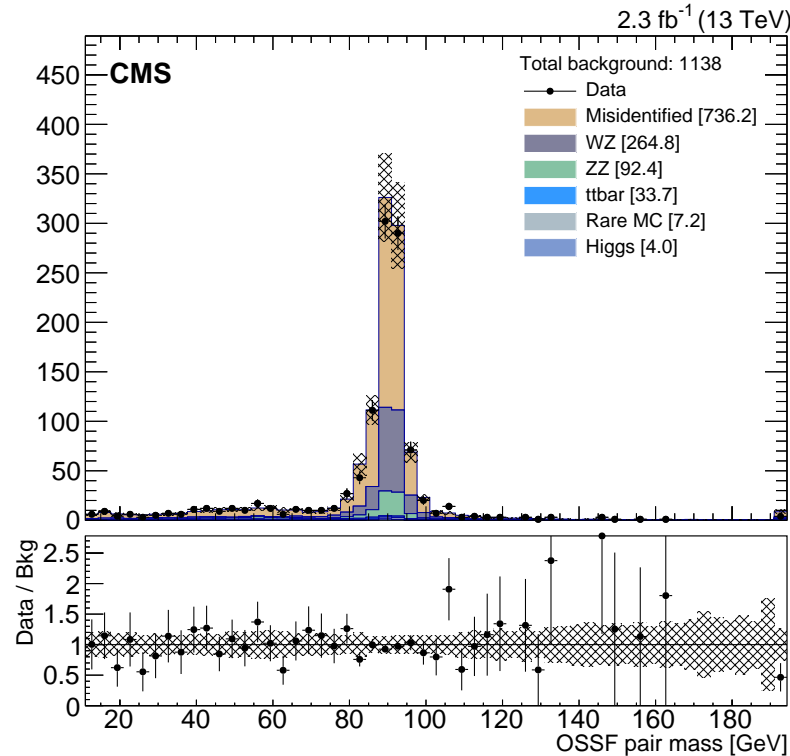
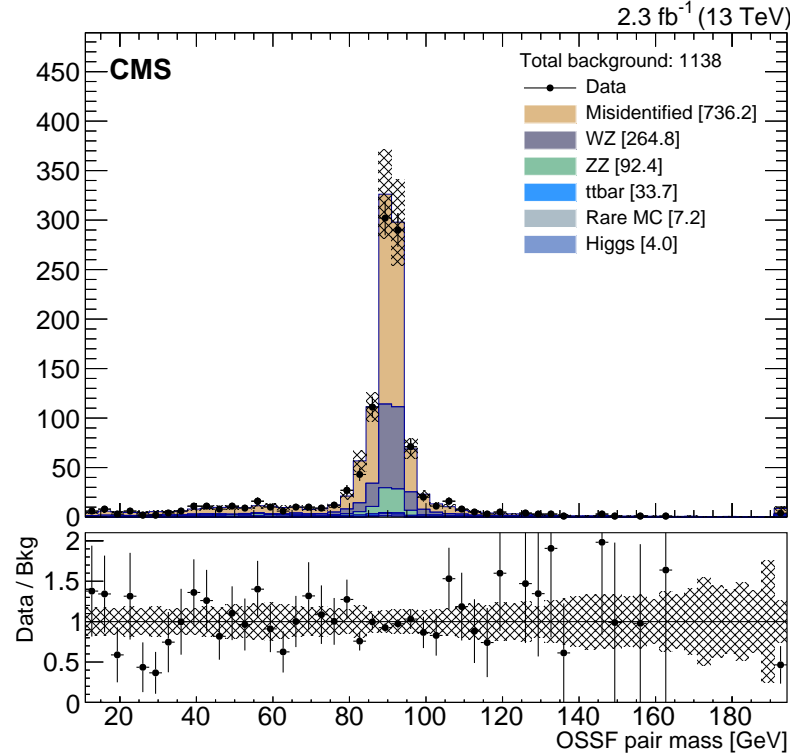


Figure 6.1: $m_{\ell\ell}$ distribution in the dilepton fake region (off-Z, trilepton events with $m_{\ell\ell\ell}$ on Z have been vetoed).

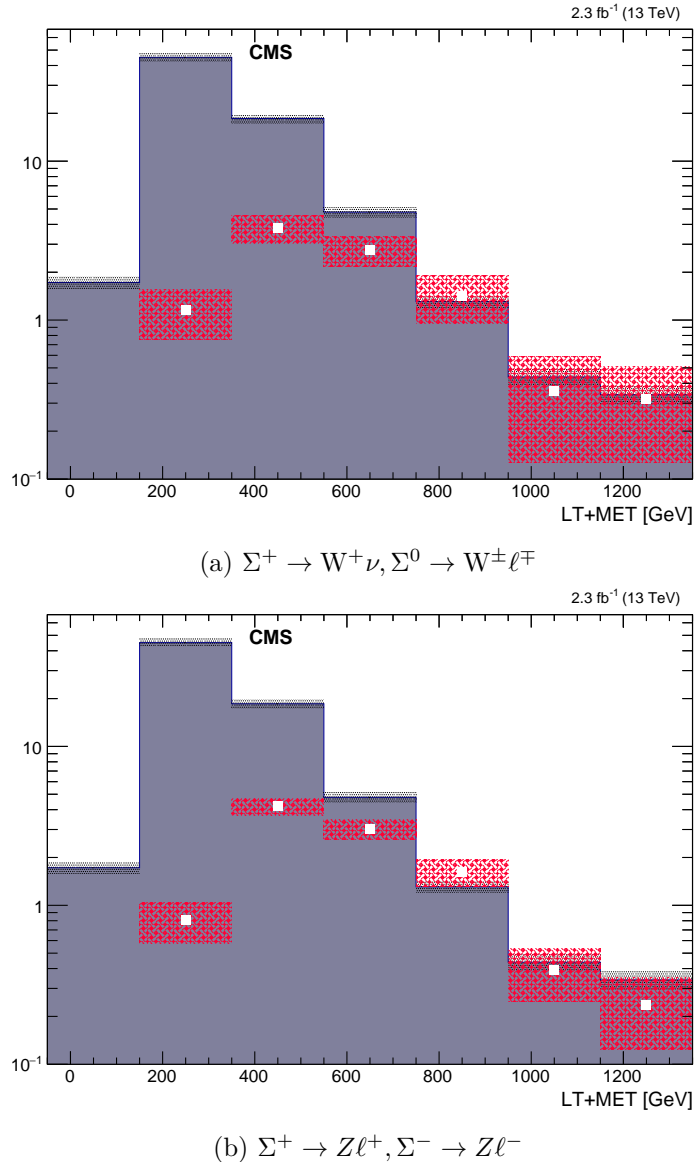


Figure 6.2: $L_T + E_T^{\text{miss}}$ shape for two different production and decay modes at $m_\Sigma = 340 \text{ GeV}$, with WZ background. Signal normalization arbitrary (for illustration purposes only).

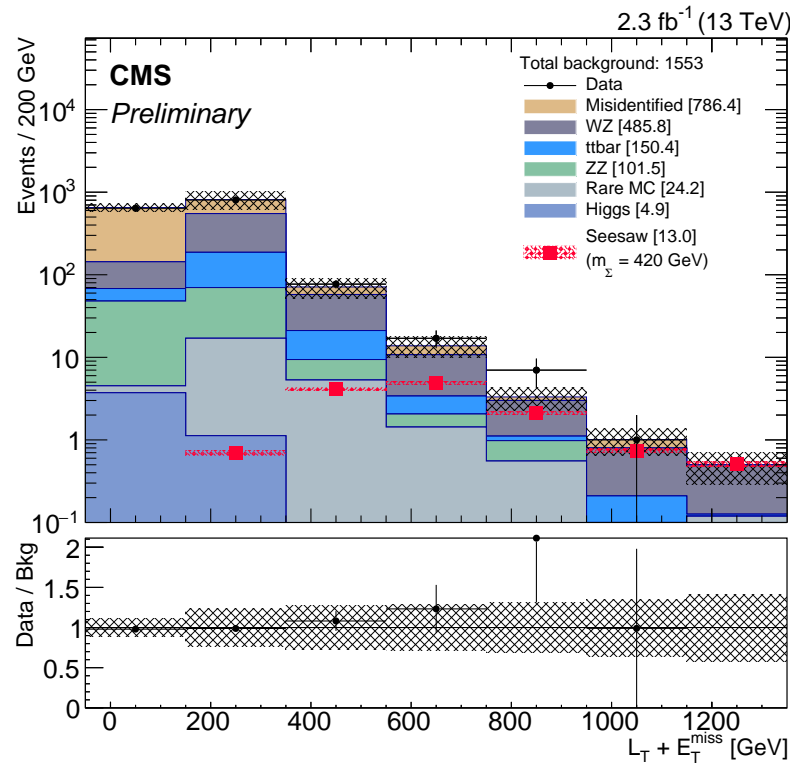


Figure 6.3: $L_T + E_T^{\text{miss}}$ distribution after event selection cuts from Sec. 5.2, to illustrate the signal separation power of this variable (last bin includes overflow). Backgrounds are described in Chapter 7. The signal ($m_\Sigma = 420 \text{ GeV}$, sum of all production and decay modes) is shown as white square dots with a pink hashed uncertainty band. The background uncertainty is specified by the gray band. Uncertainty bands include both statistical and systematic uncertainties. Numbers in square brackets denote the number of events contributed by each process.

Table 6.1: Signal Regions. Overlap with control regions removed everywhere.

n_{leptons}	OSSF pair	$L_T + E_T^{\text{miss}}$ [GeV]
3	none	
	on-Z	
	above-Z	350..1150 in steps of 200, plus overflow
≥ 4	≥ 1	350..1150 in steps of 200, plus overflow

The optimum requirement on $L_T + E_T^{\text{miss}}$ depends on the mass of the heavy fermions. In order to separate the signal as well as possible from the background, we categorize the data in bins of $L_T + E_T^{\text{miss}}$, regardless of the particle mass. We use 4 bins of width 200 GeV starting at 350 GeV, plus an overflow bin. Below 350 GeV, the amount of signal is insignificant in comparison to the background.

We remove any overlap with background control regions by explicitly vetoing the control region selections. Furthermore, we discard the below-Z trilepton region and the four-lepton region without an OSSF pair because, with the given amount of luminosity, they contain a negligible amount of signal and thus do not contribute to the sensitivity.

As a result, we have four $L_T + E_T^{\text{miss}}$ distributions, depending on the lepton properties: 3 leptons without OSSF pair, 3 leptons with OSSF pair on-Z, 3 leptons with OSSF pair above-Z, and 4 leptons with at least one OSSF pair. Each distribution begins at 350 GeV and reaches to 1150 GeV in steps of 200 GeV. We add an overflow bin for $L_T + E_T^{\text{miss}} > 1150$ GeV so that there are five bins per distribution. The resulting set of 20 signal regions is described in Table 6.1.

Chapter 7

Backgrounds

To judge the importance of each background, we consider the breakdown in the ten signal regions that are most sensitive to the signal. These signal regions, such as the region with three leptons, an OSSF pair on-Z, and $L_T + E_T^{\text{miss}} > 550 \text{ GeV}$, lie in the peripheral areas of the multilepton phase space and are thus limited by statistics. The most notable backgrounds are:

1. $\text{WZ} \rightarrow \ell\ell\ell\ell$. This process is responsible for about 51 % of the total background in the top ten signal regions (i.e. the 10 most sensitive bins of Fig. 9.1).
2. Fully leptonic $t\bar{t}$ decays with a fake lepton from a b-jet, 21 % of the total background.
3. $Z \rightarrow \ell\ell$ plus a fake lepton from a jet or a photon. This process makes up about 17 % of the total background.
4. $ZZ \rightarrow 4\ell$, 3 % of the total background.

The prompt diboson backgrounds (WZ and ZZ) are obtained from simulation, but normalized and validated in data control regions. For processes that contain fake leptons (Z or $t\bar{t}$ accompanied by a third lepton), fake rates are measured in appropriate control regions. The $Z + \text{fake}$ estimate is fully data-driven using a method that also covers similar, albeit smaller backgrounds like $\text{WW} + \text{fake}$. In our figures, this background is labeled “Misidentified”.

In the case of $t\bar{t}$, the process-specific kinematics are harder to capture using a fully data-driven method; we thus extract the kinematics from MC, while the fake rate remains

Table 7.1: Background control regions (left) are defined by the criteria listed at the top. S_T is the scalar sum of the lepton transverse momenta, the transverse momenta of jets, and E_T^{miss} .

	n_{leptons}	OS pair	$n_{\text{b-tags}}$	S_T [GeV]	E_T^{miss} [GeV]
$t\bar{t}$	2	1 opposite flavor	≥ 1	> 300	
Z + fake	3	1 same flavor, on-Z			< 50
WZ	3	1 same flavor, on-Z			50–150
ZZ	≥ 4	2 same flavor, at least one on-Z			< 50

data-driven. The remaining 9 % of the background are due to rare processes like $t\bar{t}Z$, $t\bar{t}W$, and $H \rightarrow 4\ell$ which we obtain directly from MC simulation. In our figures, these backgrounds are denoted “Rare MC” and “Higgs”, respectively.

Whenever MC simulation is used, we rely on the Powheg or MadGraph5_aMC@NLO generators. An overview of the control regions involved in our background studies is given in Table 7.1.

7.1 WZ Background

This is the primary background in our search (about 51 %). To estimate this process, we define the WZ control region by 3 leptons, an on-Z OSSF pair, and $50 \text{ GeV} < E_T^{\text{miss}} < 100 \text{ GeV}$. We use WZ MC with fully leptonic decays and normalize the total number of events in the control region, after subtracting other backgrounds. The normalization factor is 0.95 ± 0.07 (stat).

We validate the n_{jets} distribution in the control region (Fig. 7.1) and find that n_{jets} weights do not need to be applied. The WZ-specific shape of the transverse mass distribution (Fig. 7.2a) is checked as well, where the transverse mass M_T is defined as

$$M_T = \sqrt{2E_T^{\text{miss}} p_T^\ell \left(1 - \cos \angle(\vec{E}_T^{\text{miss}}, \vec{p}_T^\ell)\right)},$$

and ℓ refers to the lepton that is not part of the OSSF pair. In case of ambiguity, the OSSF pair is defined as the one whose invariant mass is closer to the Z boson mass.

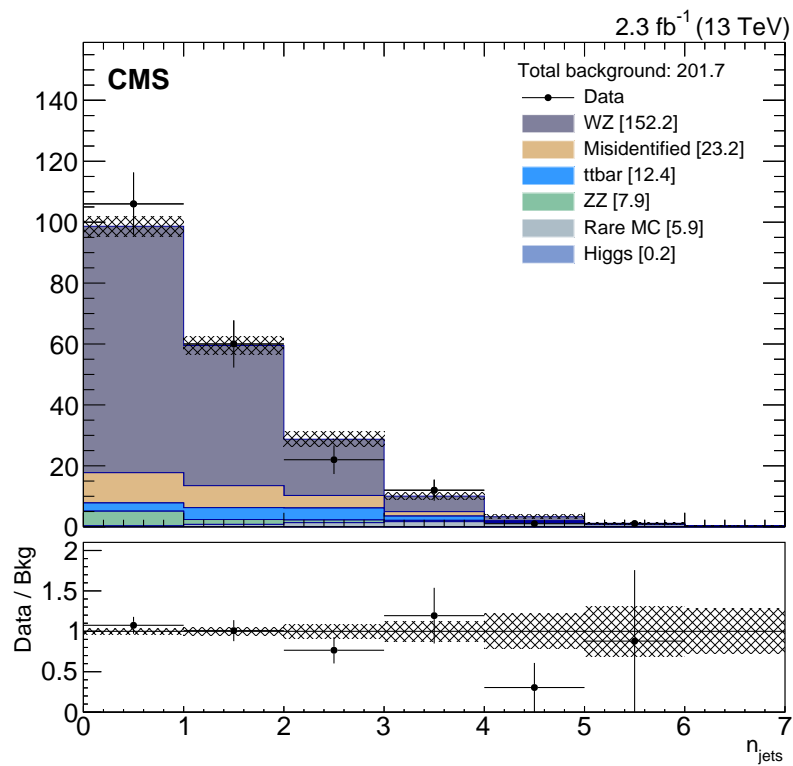


Figure 7.1: n_{jets} distribution in the WZ-dominated control region (last bin includes overflow). Uncertainty bands include both statistical and systematic uncertainties, with the exception of the WZ normalization uncertainty.

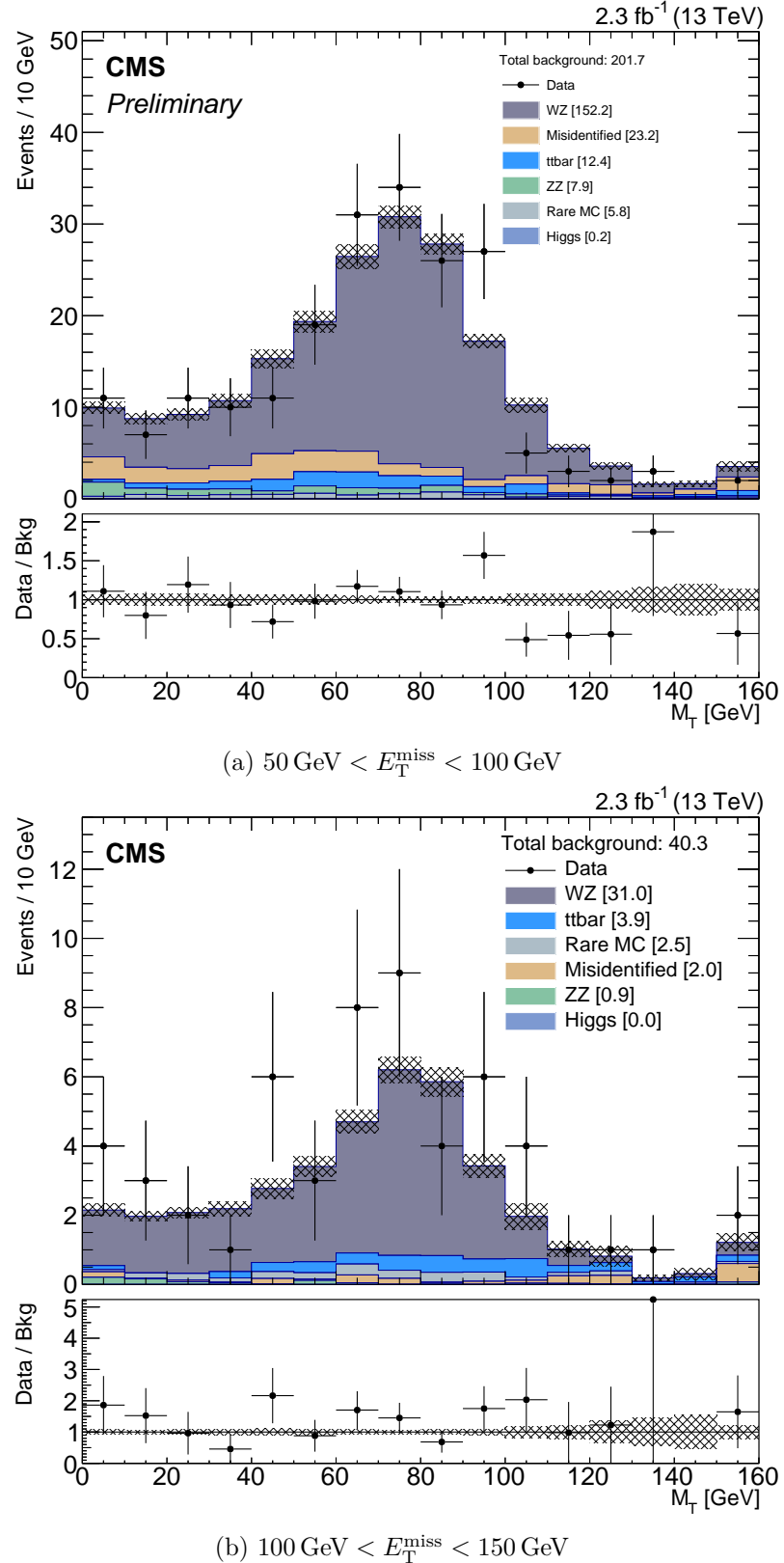


Figure 7.2: M_T distributions in the WZ-dominated control and validation regions (last bin includes overflow). Uncertainty bands include both statistical and systematic uncertainties, with the exception of the WZ normalization uncertainty.

In the adjoining $100 \text{ GeV} < E_T^{\text{miss}} < 150 \text{ GeV}$ validation region, we find that the normalization is off. Based on the amount of data investigated, we cannot tell whether this is a statistical fluctuation or a mismodeling effect. Detailed investigations of the extra events did not uncover any unexpected kinematic patterns. We thus assign a systematic uncertainty of 50% based on the variation of the normalization factor between the normalization region and the validation region (see Fig. 7.2b).

7.2 $t\bar{t}$ Background

The $t\bar{t}$ process contributes about 21% to the total background in our search. We rely on MC to model the process-specific kinematic properties. To that effect, we first verify that the simulation works well in dilepton events, and then correct the MC fake rate to match the one in data.

7.2.1 Dilepton Studies

The $t\bar{t}$ control region is defined by exactly 2 opposite-sign opposite-flavor leptons ($e^\pm \mu^\mp$), at least 1 b-tagged jet above 30 GeV, and $S_T > 300 \text{ GeV}$, where S_T is the scalar sum of the lepton transverse momenta, the transverse momenta of jets with $p_T \geq 30 \text{ GeV}$ and $|\eta| \leq 2.4$, and E_T^{miss} . We use this region to normalize the background prediction; the normalization factor is $0.80 \pm 0.01 \text{ (stat)}$.

We also use this control region to derive weights in bins of n_{jets} (see Fig. 7.3). The corrections typically range between 1% and 10%. Note that, as we do not bin our signal regions in jet-related quantities, the impact of these weights on the results is negligible. Still, as the n_{jets} distribution was seen to be in disagreement, weights were applied to improve the general accuracy of the simulation.

The E_T^{miss} and S_T distributions after normalization and weights are shown in Fig. 7.4.

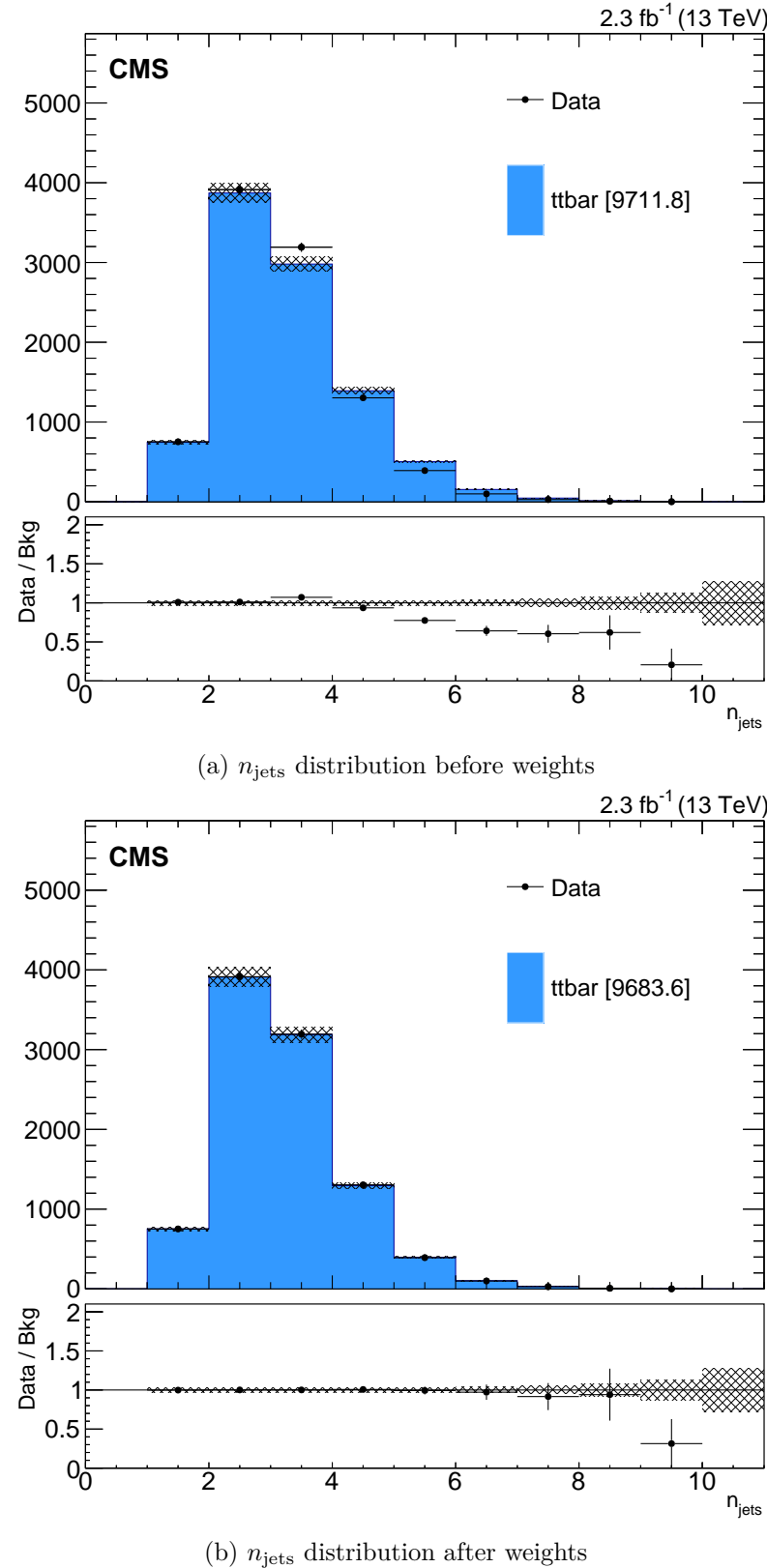


Figure 7.3: n_{jets} distributions in $t\bar{t}$ -dominated control region (last bin includes overflow). Uncertainties are statistical only.

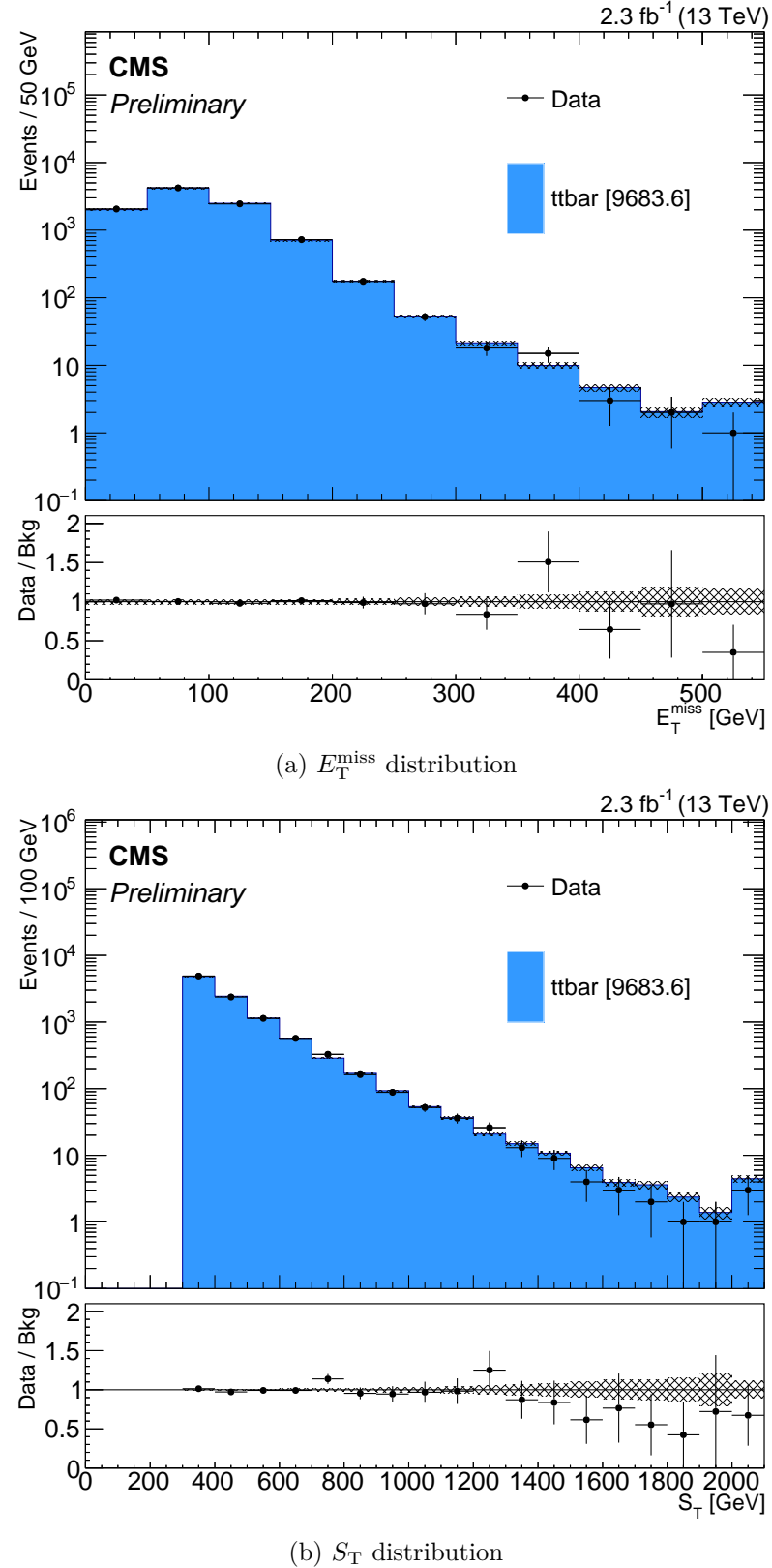


Figure 7.4: Kinematic distributions in $t\bar{t}$ -dominated control region (last bin includes overflow). Uncertainties are statistical only.

7.2.2 Trilepton Studies

Having established the validity of kinematic aspects of the $t\bar{t}$ simulation using the dilepton (prompt) sample, we verify that also the rate at which the $t\bar{t}$ MC produces trilepton events is in agreement with that rate in data. To this end, we measure the lepton fake rate in a sample dominated by semi-leptonic $t\bar{t}$ decays. This sample is selected by requiring one tight muon with $p_T > 30 \text{ GeV}$, 2 jets (from the other top quark), one additional b-tagged jet, and a non-prompt lepton which is most likely fake.

We find the $t\bar{t}$ fake rate in data to be $1.5 \pm 0.5 \text{ (stat)}$ times the one found in the $t\bar{t}$ simulation. This indicates that the number of events with fake leptons is underpredicted in the $t\bar{t}$ simulation. We thus use this ratio to correct the number of predicted trilepton events from $t\bar{t}$ and apply a systematic uncertainty of 50 %.

7.2.3 Dilepton + Track Studies

The prediction for the $Z + \text{jets}$ background (Sec. 7.3) uses isolated tracks as a handle to estimate the number of fake leptons from jets. However, some of these tracks may come from $t\bar{t} + \text{jets}$ production, so that the two methods overlap. To avoid overpredicting the background in the $Z + \text{jets}$ method, the number of tracks as predicted by the $t\bar{t}$ simulation is subtracted before calculating the track-based estimate. The reliability of this procedure depends on the accuracy of the track modeling in simulation.

We therefore verify that the number of tracks from $t\bar{t}$ is predicted correctly, by comparing both the distributions of non-isolated tracks and of isolated tracks in the dilepton control region. While the former, shown in Fig. 7.5a, agrees well with the data and gives us confidence in the general quality of the simulation, the latter shows disagreement in the bins with at least one isolated tracks (Fig. 7.5b). We therefore scale the number of tracks from the $t\bar{t}$ simulation by a factor of 1.5.

Considering both plots in Fig. 7.5 together suggests that the $t\bar{t}$ simulation does not model the track isolation distribution distribution correctly. As the mismodeling of the $t\bar{t}$ fake rate

(Sec. 7.2.2) is quantitatively and qualitatively similar, it is likely that both discrepancies have a common cause in the simulation. We therefore apply the same systematic uncertainty (50 %) to the track prediction.

Further details on the Z + jets background estimation can be found in Sec. 7.3.

7.3 Z + fake Background

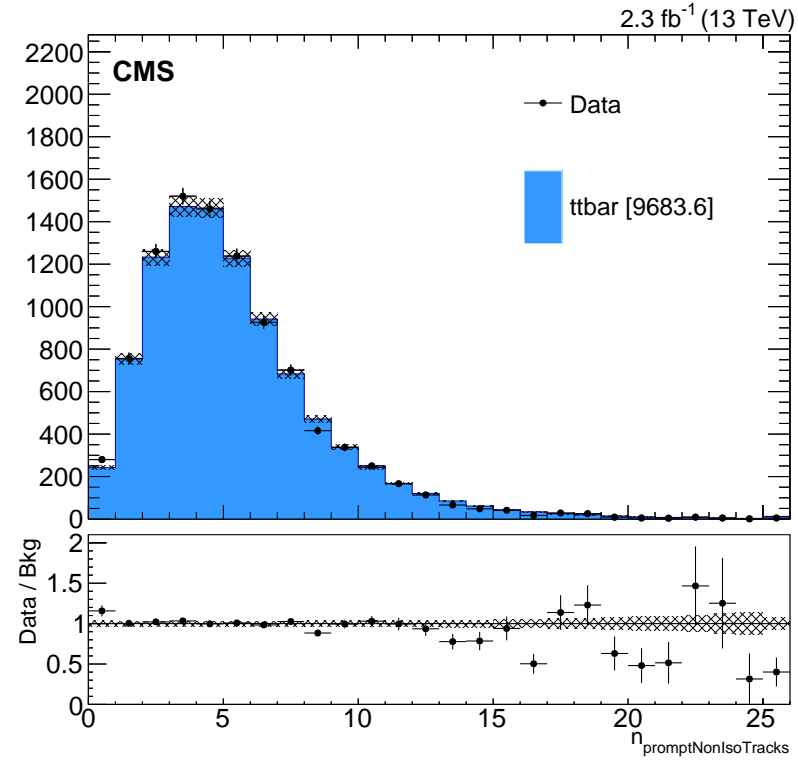
The Z + fake process contributes about 17 % of the total background. Since the fake leptons are not modeled with sufficient precision by simulation, we employ a data-driven method that uses correlated objects in order to predict the Z + fake (“misidentified”) background.

7.3.1 Method

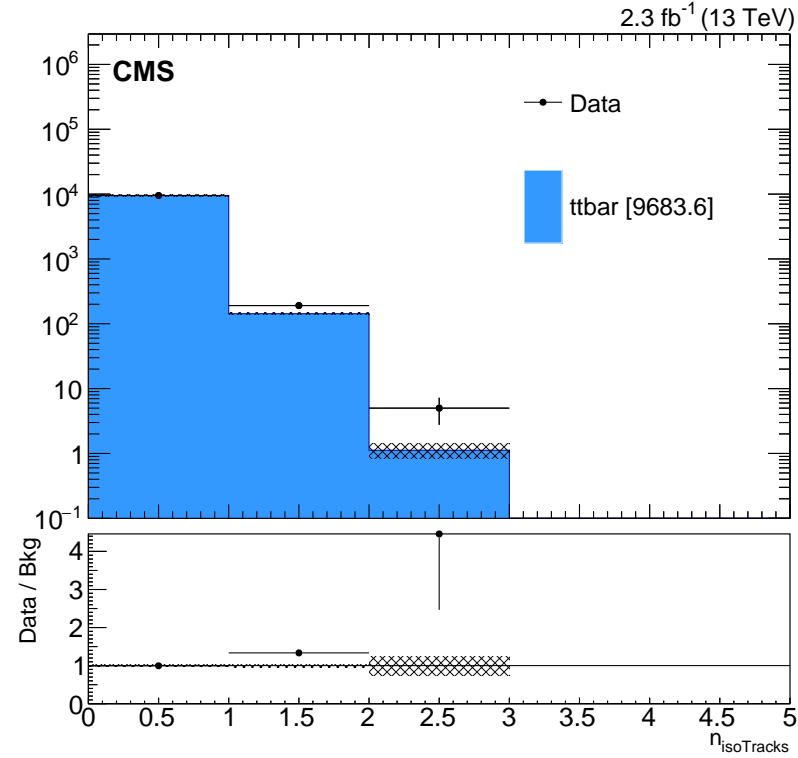
To determine the background with fake electrons and muons, we rely on looser objects measured in data that are emitted in a similar way in the decay chain and are therefore expected to be correlated with the fake leptons, and use them as lepton proxies.¹ We verify that the kinematic properties of these proxies resemble those of the fake leptons. We then generate a fake sample based on the $2\ell+[\text{proxy object}]$ data, treating the proxy objects as leptons (“seed sample”). Further down in the analysis chain, these fake leptons simply appear as regular leptons (e.g. when computing invariant masses). Proxy objects that can take multiple roles are considered the appropriate number of times (see below).

The number of 3ℓ events in data per $2\ell+[\text{proxy object}]$ event in this fake sample is then evaluated (“fake rate”). With the help of the fake rate, we predict the background in the signal regions, by applying it to the corresponding seed sample which requires one less lepton and a proxy object instead. Because the proxy objects appear as leptons, this is simply done by selecting the signal region from the fake sample and multiplying the yield by the fake rate.

¹These looser objects are not necessarily leptons as well. For example, a photon that converts into two leptons, one of which has very low p_T , may have kinematics which are very similar to the ones of the other conversion lepton that carries most of the p_T . (Of course, the selection of such objects may be tricky.)



(a) Number of non-isolated tracks



(b) Number of isolated tracks

Figure 7.5: Track distributions in $t\bar{t}$ -dominated control region (last bin includes overflow). Uncertainties are statistical only.

To compute the fake rate $\frac{N(3\ell)}{N(2\ell+[\text{proxy object}])}$, we subtract contributions from other backgrounds in the numerator and the denominator. This step interacts with the MC background normalizations and thus requires an iterative process to converge. The fake rate then describes the number of fake leptons as a fraction of the number of $2\ell+[\text{proxy object}]$ events from all processes that have not been modeled otherwise.

When we apply the fake rate in a signal region, we multiply it by the total number of $2\ell+[\text{proxy object}]$ events found in the corresponding seed region in data. However, we use MC to obtain the fake contribution for certain backgrounds.² In these cases, double-counting needs to be mitigated. Therefore, we take the $2\ell+[\text{proxy object}]$ component of the background MC sample, apply the same fake rate as for data, and subtract the resulting prediction from the regular data-driven prediction (see e.g. Sec. 7.2 for $t\bar{t}$). This is equivalent to keeping the seed sample clean of proxies originating from processes that are modeled otherwise. We therefore verify that the number of tracks be modeled correctly in MC (see Sec. 7.2.3).

In rare cases due to statistical fluctuations, the subtraction might yield a (small) negative number. If that happens, we replace it by zero, to make sure that the background prediction behaves physically reasonably.³ For technical details, see Appendix B.3.

7.3.2 Fake Leptons from Asymmetric Internal Photon Conversions (AIC)

We look at the number of events that have 3 light leptons (no τ_{had}) including an OSSF pair below Z (i.e. $m_{\ell\ell} < 81 \text{ GeV}$), no b-tags, $H_T < 200 \text{ GeV}$, and $E_T^{\text{miss}} < 50 \text{ GeV}$. This is essentially the Z peak region, except that the dilepton invariant mass is not large enough to fall on the Z peak, and a third lepton is present.

This region primarily contains events from $Z \rightarrow \ell\ell$ where one of the final state leptons

²This is especially important for $t\bar{t}$ when a b-tag is not present, since the fake rate is higher in $t\bar{t}$ events, but there is no obvious way to discern these events from non- $t\bar{t}$ events in the seed sample.

³Another option would be to subtract the MC-fake-seed-driven background from the regular $t\bar{t}$ MC prediction (again with a lower bound at 0). However, 8 TeV cross-checks have shown that this leads to less accurate results.

radiates an off-shell photon which decays, or—equivalently—internally converts, asymmetrically to two additional leptons, one of which carries very low p_T and is not reconstructed as an independent object in the detector. The process of emission of an off-shell photon through asymmetric internal conversion (AIC) then yields a single reconstructed lepton in the detector [49]. Since the p_T of the lost lepton is low, the leading three leptons nearly reconstruct the invariant mass of the Z peak. The internal conversion process has an infrared singularity, so the distribution of off-shell photon masses is peaked at very low values. The resulting kinematic distribution in this region of phase space is then very similar to the emission of a real on-shell photon.

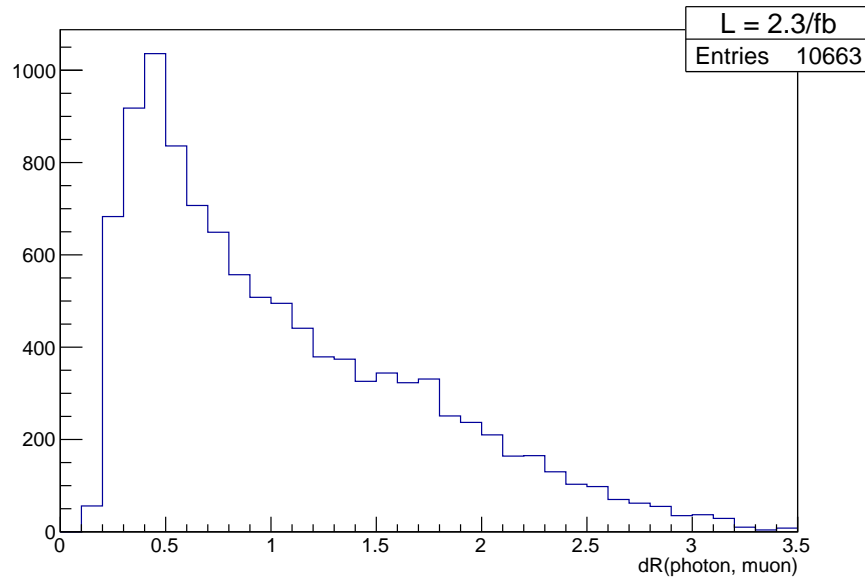
We may therefore form a seed sample with photons as proxies for fake leptons coming from asymmetric internal conversion. All combinations are taken into account, i.e. dilepton events with a photon enter the fake sample as four event types (two possible flavors, two possible charges). The photons are required to be within $0.30 \leq \Delta R \leq 0.60$ from another light lepton. This is the characteristic distance for radiated photons of the type considered, as can be seen from Fig. 7.6.

Looking in the seed sample, we find that the $2\ell + \gamma$ mass indeed reproduces the Z peak, as shown in Fig. 7.7. For photons faking muons, we find better shape agreement if we apply a loss factor of 0.8 to the photon p_T when creating the fake trilepton sample, attributing an average of 20 % of the p_T to the lost lepton. Outside the trilepton Z window, it is necessary to increase the fake rate by 1.8 to achieve agreement.

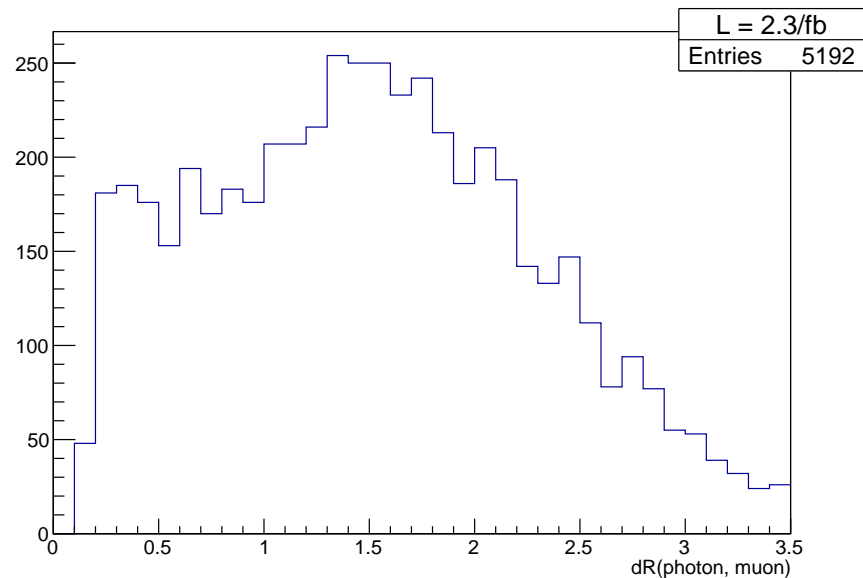
After these corrections, we find that the photon fake rates are

- muons: 1.60 % (ee environment), 1.05 % ($\mu\mu$ environment),
- electrons: 3.5 % (ee environment), 4.5 % ($\mu\mu$ environment).

We apply a 52 % systematic uncertainty on the total photon-based background estimate to cover the variation of observed fake rates as a function of the flavor of the remaining prompt lepton pair in the event.

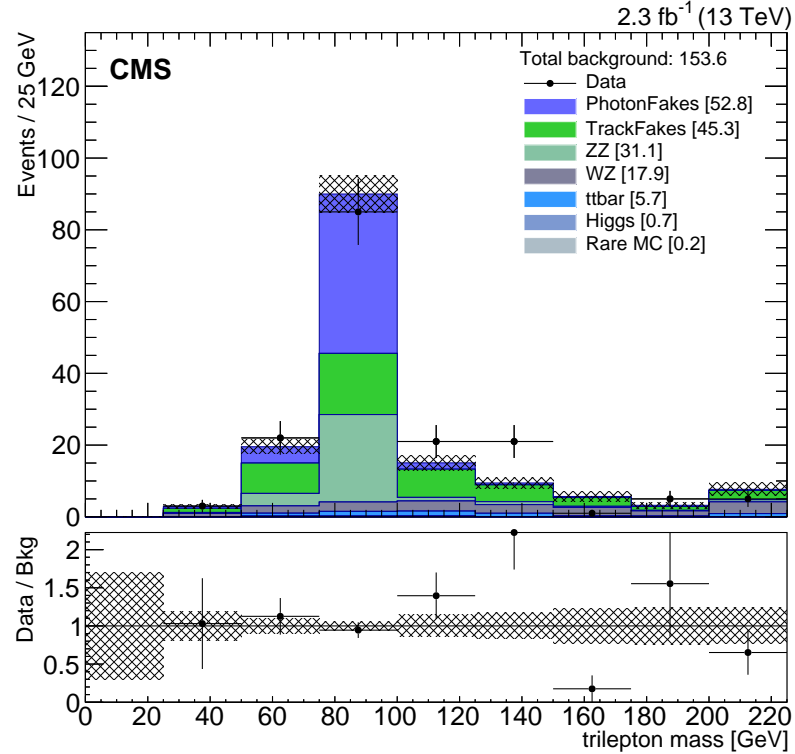


(a) dilepton AIC control region (OSSF pair below-Z)

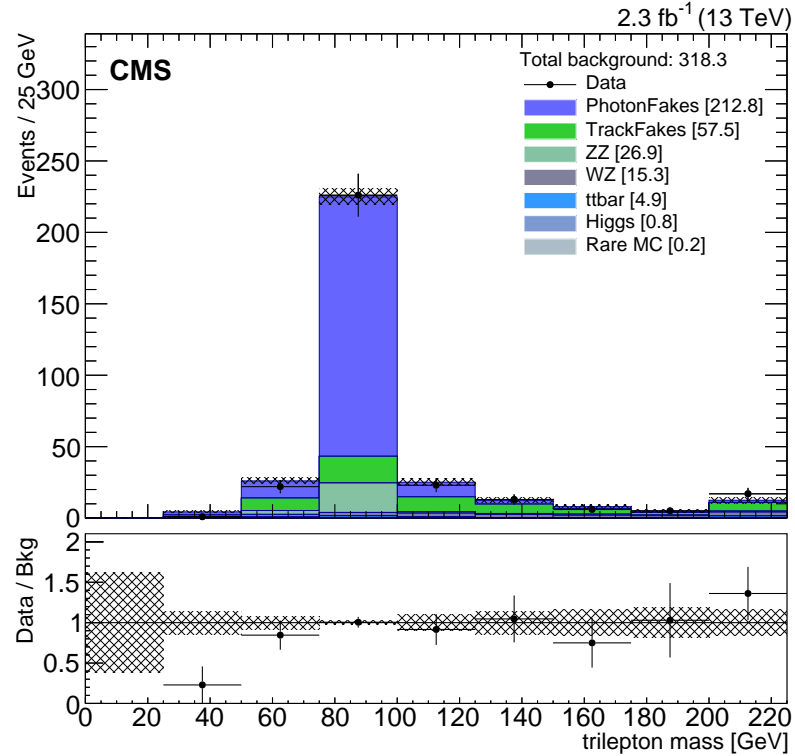


(b) dilepton region on-Z

Figure 7.6: ΔR distributions between photon and muon.



(a) fake muon



(b) fake electron

Figure 7.7: $m_{3\ell}$ distribution in AIC-dominated control region.

7.3.3 Fake Leptons from Jets

In order to determine the background with fake electrons and muons from jets, we use isolated tracks as proxies. The isolation criteria that we require these tracks to satisfy are identical to our muon isolation criteria (see Sec. 5.1). We produce a track-based fake 3ℓ background seed sample by reassigning isolated tracks to the lepton collections, so that the sample has one less lepton than the signal regions and an isolated track instead. All combinations are taken into account, i.e. tracks are used to create both a fake- e and a fake- μ event.⁴ The fake background can then be estimated by applying the fake rate after requiring the signal region selection in this seed sample.

The fake rate $\frac{N(3\ell)}{N(2\ell+\text{track})}$ is determined using events with 3 electrons or muons including an OSSF pair on-Z and $E_T^{\text{miss}} < 50 \text{ GeV}$. This is the prominent Z peak region with an additional lepton. As we subtract contributions from other backgrounds in the numerator and the denominator, this fake rate describes the number of fake leptons as a fraction of the number of $2\ell + \text{track}$ events from all processes that are not modeled otherwise.

To achieve the best possible modeling, we make sure that the kinematic properties of the isolated tracks in this region resemble those of the fake leptons by applying weights to the track-based background in bins of the the lowest p_T lepton (proxy) which is generally the fake (Fig. 7.8). Appendix A contains additional plots supporting the suitability of tracks as lepton proxies. We then measure the number of 3ℓ events in data per $2\ell + \text{track}$ event (fake rate), as a function of the flavor of both the fake lepton and of the Z decay products and find:

- muons: $(1.49 \pm 0.21) \%$ (ee environment), $(1.49 \pm 0.17) \%$ ($\mu\mu$ environment),
- electrons: $(1.37 \pm 0.22) \%$ (ee environment), $(1.75 \pm 0.19) \%$ ($\mu\mu$ environment).

Based on this, we use the electron and muon fake rates $(1.59 \pm 0.15 \text{ (stat)}) \%$ and $(1.49 \pm$

⁴Multiple fakes in an event are not considered (neither of same proxy type (e.g. two tracks) nor of different type). Hybrid fakes (one from a track, one from a photon) are currently not supported for technical reasons; same-type fakes however turned out to cause problems with the $t\bar{t}$ MC subtraction. Given the smallness of the fake rates ($O(10^{-2})$), the contribution from multiple fakes is negligible anyways.

$0.13(\text{stat})\%$, respectively. We apply a systematic uncertainty of 14% to cover the variation of observed fake rates as a function of the flavor of the remaining prompt lepton pair in the event.

To apply the fake rate in a signal region, we multiply it by the total number of events found in the corresponding $2\ell + \text{track}$ region in data. However, since we use MC to obtain the fake contribution for the $t\bar{t}$ background, we need to correct for double-counting. We thus subtract the contribution from $2\ell + \text{track}$ events as predicted by the $t\bar{t}$ MC from the data. To show that the subtraction is valid, we verify that the n_{tracks} distribution in the $t\bar{t}$ MC sample matches the one in data, so that we can trust the fake rate method used in data is applicable for the $t\bar{t}$ MC subtraction (see Sec. 7.2).

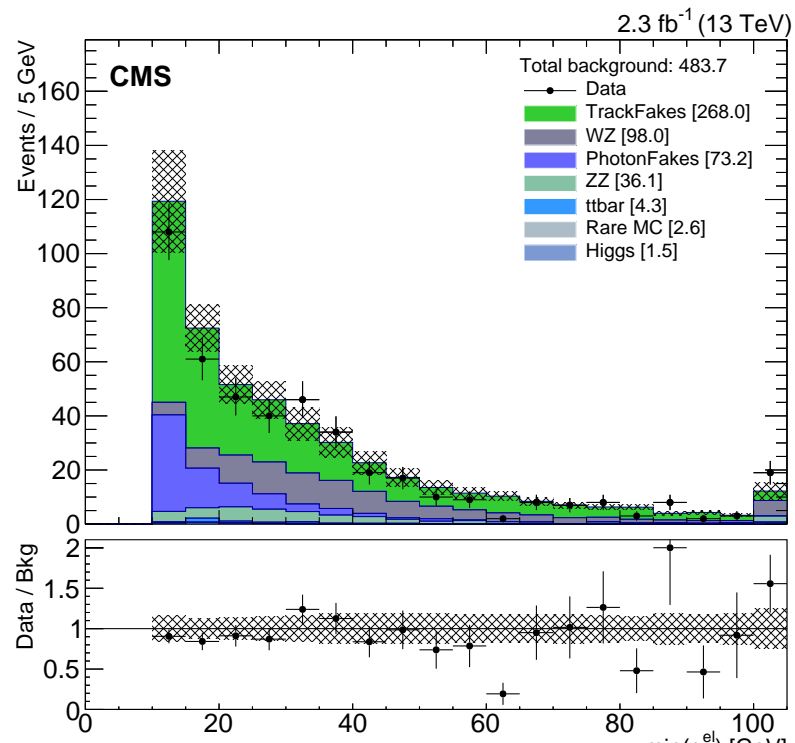
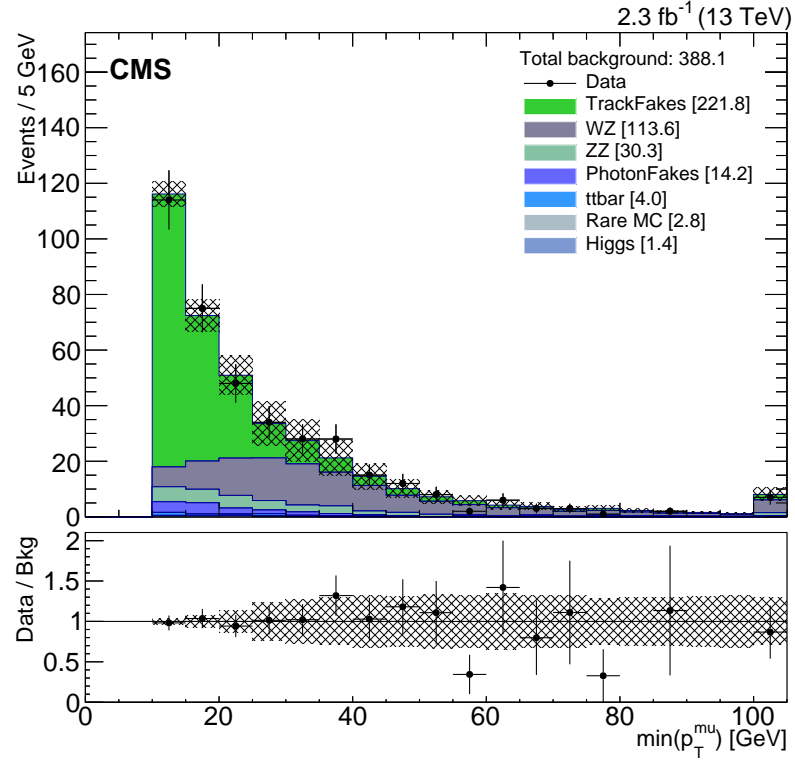
Fig. 7.9 shows the mass distribution of the “best” OS dilepton pair across its full range in the trilepton control region, both with and without an AIC veto (for off-Z events whose 3ℓ invariant mass is on Z); Fig. 7.10 distinguishes by flavors. In case of ambiguity, the “best” OS dilepton pair is the one whose invariant mass is closest to the Z mass, with the additional condition that pairs above the Z window are not considered if there is a pair below the Z window (thus shifting events from high-Z to low-Z, for a more separative background categorization, see Sec. 6.1).

As an additional cross-check, we show the H_T distribution in the Z region (Fig. 7.11). Finally, we perform a closure test in Drell-Yan MC, comparing the on-Z and off-Z behavior in the control trilepton region (see Fig. 7.12). We find that the fake rates agree within 5% on and off Z. The statistical uncertainty of the numerator in the high-Z region is 15%.

7.4 ZZ Background

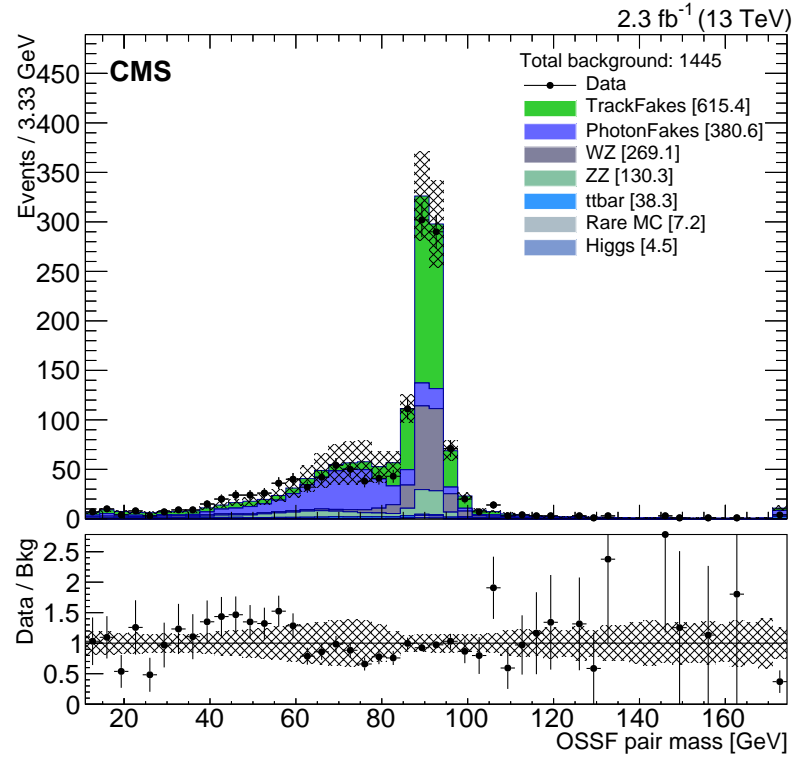
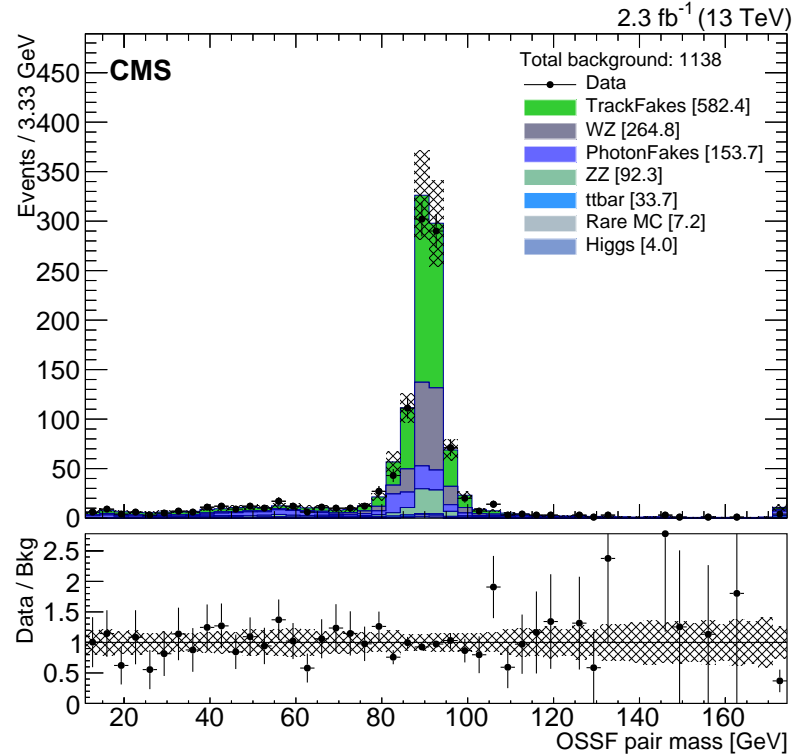
While the ZZ background is responsible for only 3% of the background in the ten channels with highest overall sensitivity, its contribution is around 40% in the 4-lepton regions.

The control region is defined by 4 leptons, 2 OSSF pairs (at least one on-Z), and $E_T^{\text{miss}} < 50 \text{ GeV}$. We use ZZ MC with fully leptonic decays and normalize the total number



(b) fake electron

Figure 7.8: p_T distributions of the lowest p_T lepton.

(a) including events with $m_{\ell\ell\ell}$ on-Z(b) events with $m_{\ell\ell\ell}$ on-Z removed from the dilepton-off-Z regionsFigure 7.9: $m_{\ell\ell}$ distribution in the dilepton + fake region.

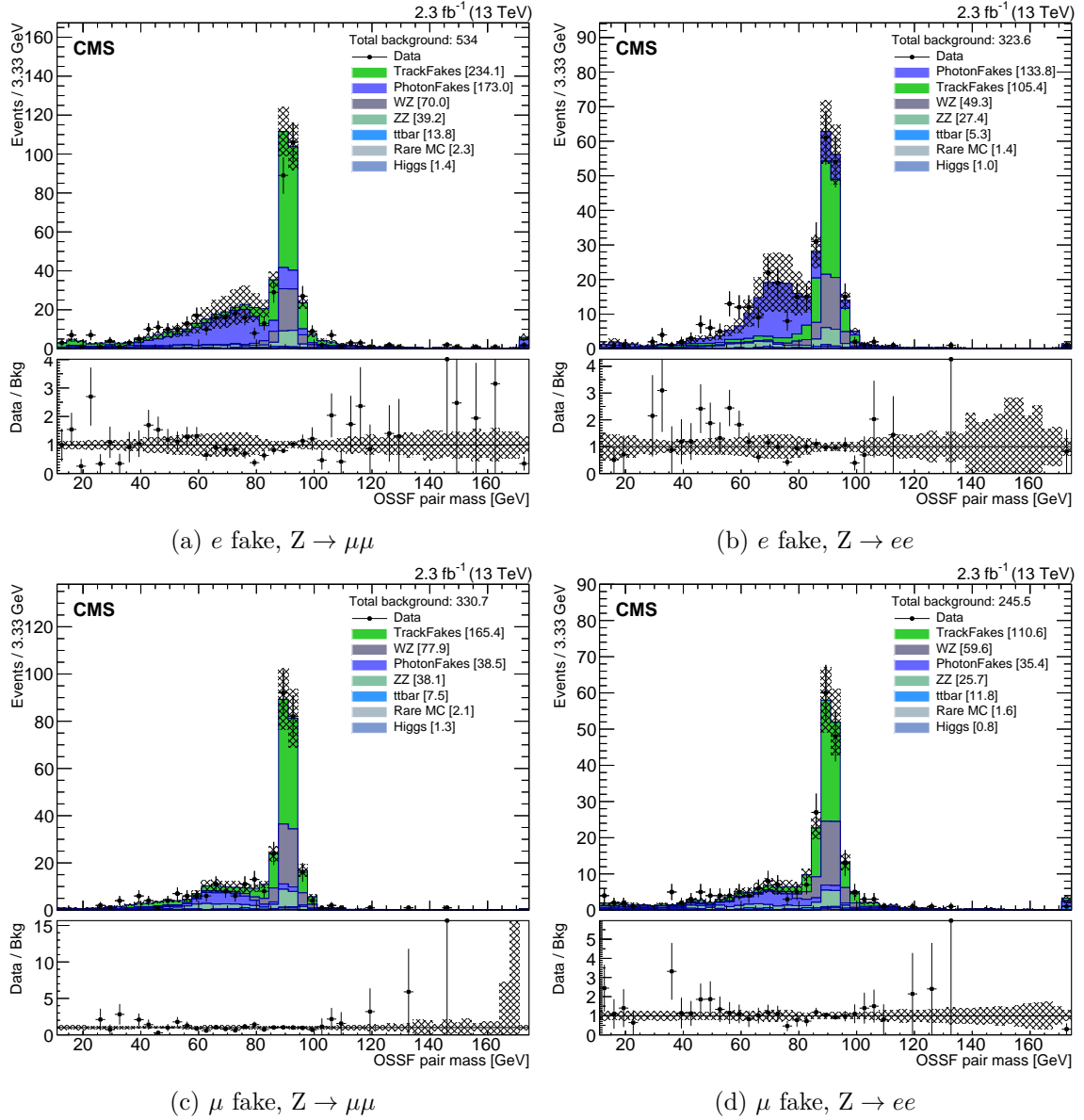


Figure 7.10: $m_{\ell\ell}$ distribution in the dilepton + fake region by flavor.

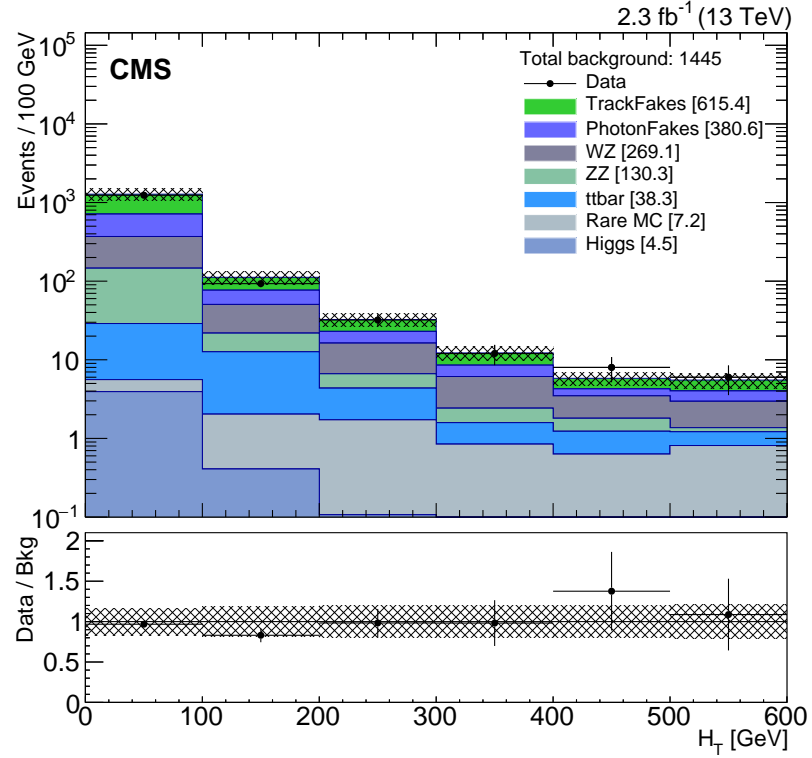


Figure 7.11: H_T distribution in the dilepton fake region (no OSSF pair mass cut).

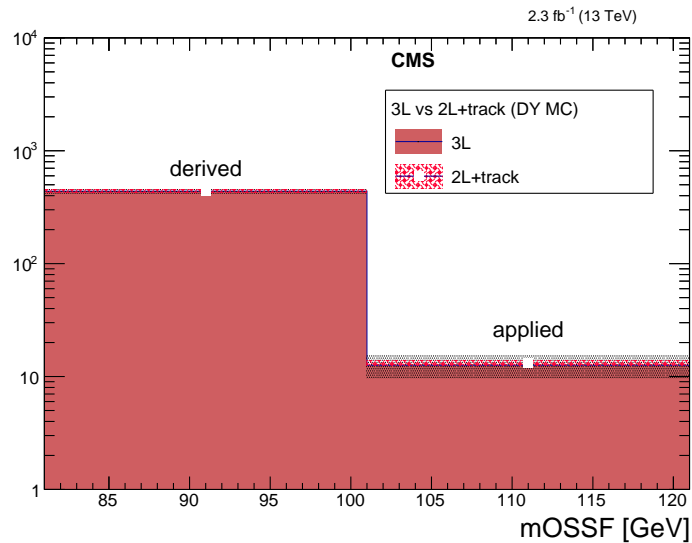


Figure 7.12: Closure test in Drell-Yan MC for the track-based fake rate method. The plot compares the 3-lepton yield with the prediction from 2 leptons + track proxy. The second bin in this plot ranges from 101 GeV to infinity.

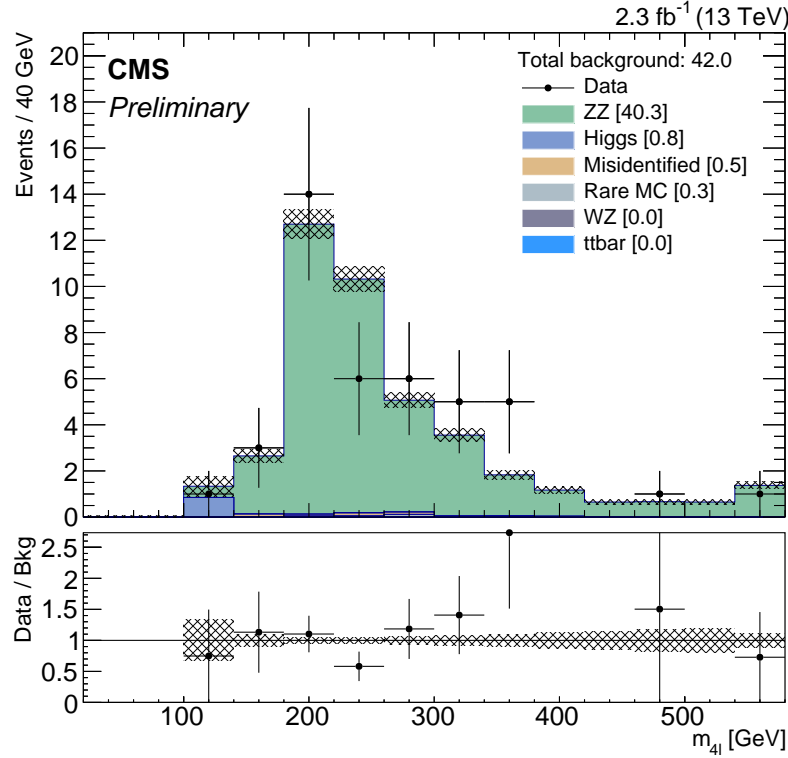


Figure 7.13: The m_{4l} distribution in the ZZ control region. The last bin is the overflow. Uncertainty bands include both statistical and systematic uncertainties, with the exception of the ZZ normalization uncertainty.

of events in the control region, after subtracting other backgrounds. The normalization factor is 1.38 ± 0.23 (stat). Fig. 7.13 shows the 4ℓ mass distribution in the control region.

Chapter 8

Systematic Uncertainties

Since most of the signal regions are limited by statistics, systematic uncertainties play a minor role. The only regions where we expect 10 or more events are the signal regions with 3 leptons including an OSSF pair on or above-Z, and $L_T + E_T^{\text{miss}} < 550 \text{ GeV}$. In these regions, the WZ and $t\bar{t}$ background uncertainties become relevant. However, channels with higher $L_T + E_T^{\text{miss}}$ are more sensitive to the signal. The full list of uncertainties is found in Table 8.1, along with their impact on a representative set of three of the most sensitive channels.

The ZZ and $t\bar{t}$ uncertainties are based on the statistical uncertainties of the normalization regions; cross section uncertainties are thus not applied. For WZ, we apply a 50 % uncertainty to account for the variation of the normalization factor depending on the E_T^{miss} range chosen for normalization (see Sec. 7.1). For rare background processes, we apply a 50 % theory systematic uncertainty to cover both PDF as well as renormalization and factorization scale uncertainties. In the case of the signal, these uncertainties are covered by a 10 % systematic uncertainty [15].

For the E_T^{miss} smearing procedure, a conservative uncertainty is determined by varying the amount of smearing by 50 %. Pile-up weights are evaluated by varying the minimzm-bias cross section by 5 % and propagating the impact on the pile-up weights through the analysis chain.

In general, systematic uncertainties are found by weighing events up or down or smearing them, then propagating those changes into the various bins of the analysis. The change in the expected backgrounds or signal yields in each bin corresponds to a systematic uncertainty,

Table 8.1: Systematic uncertainties. The channels listed here have three leptons and $550 \text{ GeV} < L_T + E_T^{\text{miss}} < 750 \text{ GeV}$.

Source of uncertainty	Magnitude	Impact on background/signal estimate in channel with		
		no OSSF pair	OSSF pair above-Z	OSSF pair on-Z
WZ normalization	50 %	13 %	2.8 %	41 %
ZZ normalization	16 %	0.1 %	0.5 %	0.4 %
Integrated luminosity	2.7 %	0.6 %	0.2 %	0.3 %
Lepton ID and isolation	3 %	3 %	3 %	3 %
E_T^{miss} resolution/smearing	50 %	4.1 %	6.3 %	0.6 %
Pile-up reweighting	5 %	1.5 %	0.3 %	1.3 %
$t\bar{t}$ fake rate	50 %	21 %	11 %	1.8 %
Z + fake rate	14 %	9.2 %	1.1 %	1.0 %
AIC fake rate	52 %	5.4 %	1.1 %	0.8 %
Rare MC cross section	50 %	11 %	2.7 %	5.2 %
Signal cross section	10 %	10 %	10 %	10 %
Total Background (for comparison)		0.3 events	3.0 events	3.5 events
Signal ($m_\Sigma = 420 \text{ GeV}$, for comparison)		0.8 events	1.8 events	0.8 events

where we keep track of the relative sign of changes between different bins in order to take correlations and anti-correlations into account. Examples:

- The luminosity uncertainty is correlated amongst all samples to which it is applied (i.e. MC samples that are not normalized to data).
- As we apply the E_T^{miss} smearing, events can migrate between $L_T + E_T^{\text{miss}}$ bins. The uncertainty of the correction is thus anti-correlated between those bins.
- An increase of the WZ normalization by 1σ leads to a decrease of the measured Z + jets fake rate, as we subtract WZ background. Similarly, a 1σ increase of the Z + jets fake rate leads to a decrease in the WZ normalization, as the two control regions cannot be completely isolated from each other and have a (small) overlap. In all these cases, we take the relative signs of the changes into account to keep track of the correlations and anti-correlations.

Details on the fake rate uncertainties can be found in Sec. 7.3.

Chapter 9

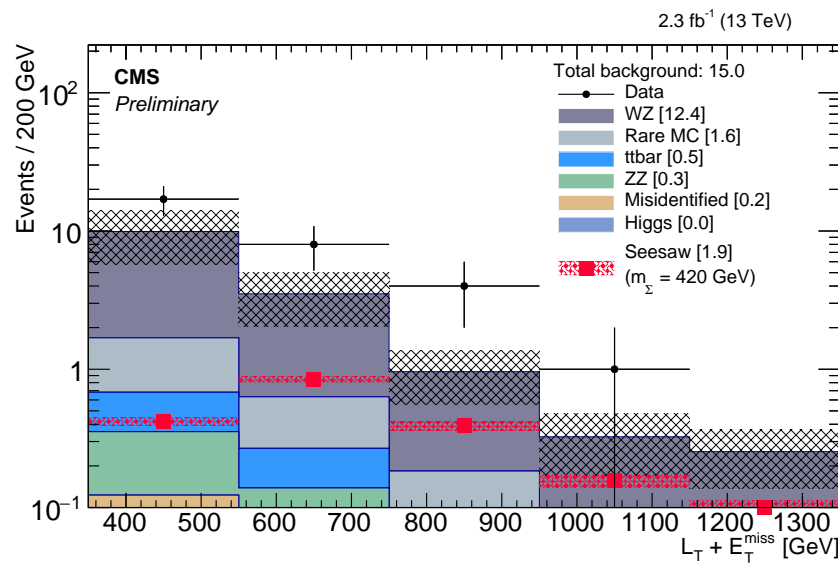
Results

9.1 Observation

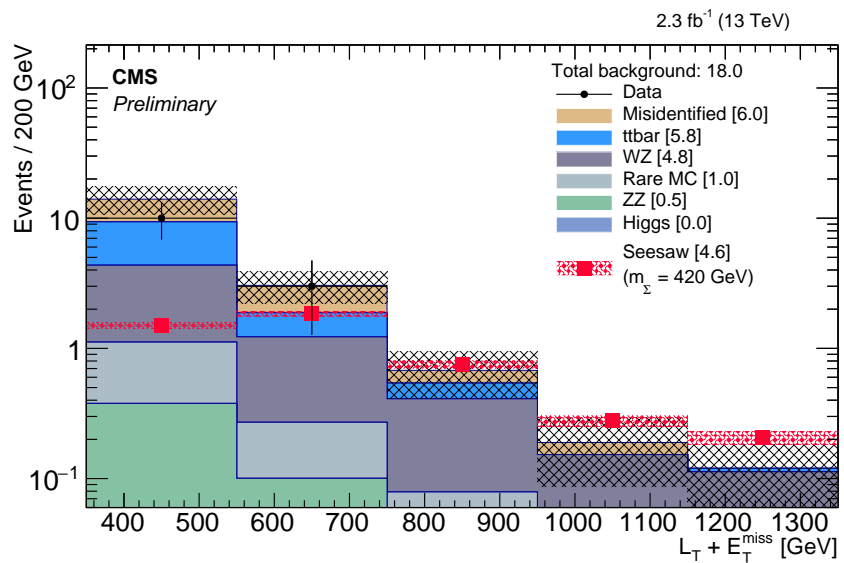
As described in Sec. 6.2 above, the $L_T + E_T^{\text{miss}}$ variable is a very efficient discriminator between the seesaw signal and the SM background. Therefore, the only requirement for the seesaw signal candidate events beyond the preliminary selection described in Sec. 5.2 is that their $L_T + E_T^{\text{miss}}$ value exceed 350 GeV. In Fig. 9.1 we present the $L_T + E_T^{\text{miss}}$ distribution for four event categories as follows: 3 leptons with OSSF pair on-Z; 3 leptons with OSSF pair above-Z; 3 leptons with no OSSF pair; 4 leptons with at least one OSSF pair. Displays of the seesaw signal for heavy fermion mass $m_\Sigma = 420$ GeV are also shown for each category. The signal generally stands out for higher values of $L_T + E_T^{\text{miss}}$, as is to be expected for a massive parent particle. The SM background decomposition is also shown for each category.

The observations are generally consistent with the SM expectations, with the possible exception of the 3-lepton category that includes an OSSF lepton pair with invariant mass consistent with that of the Z boson (Fig. 9.1a). The dominant background for this category is the WZ diboson production, as shown. Detailed investigations of the extra events did not uncover any unexpected kinematic patterns. Fig. 9.2 presents event displays for two of the events in this category.

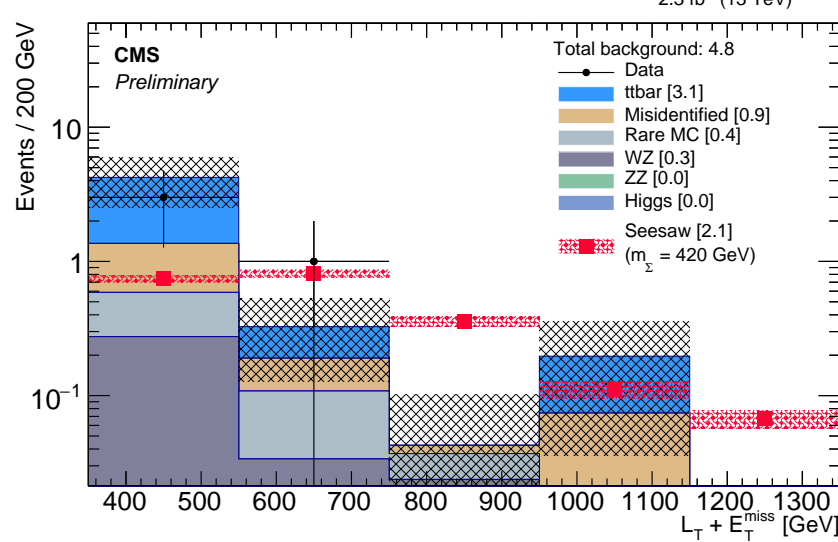
The p -value for the observation in the aggregated 20 $L_T + E_T^{\text{miss}}$ bins for the four categories shown in Fig. 9.1, assuming SM physics only, is 0.93. This overall consistency with the SM expectation conveys the message that the excess of observed events in the Fig. 9.1a is either a statistical artifact or a discrepancy that can be addressed only with additional data.



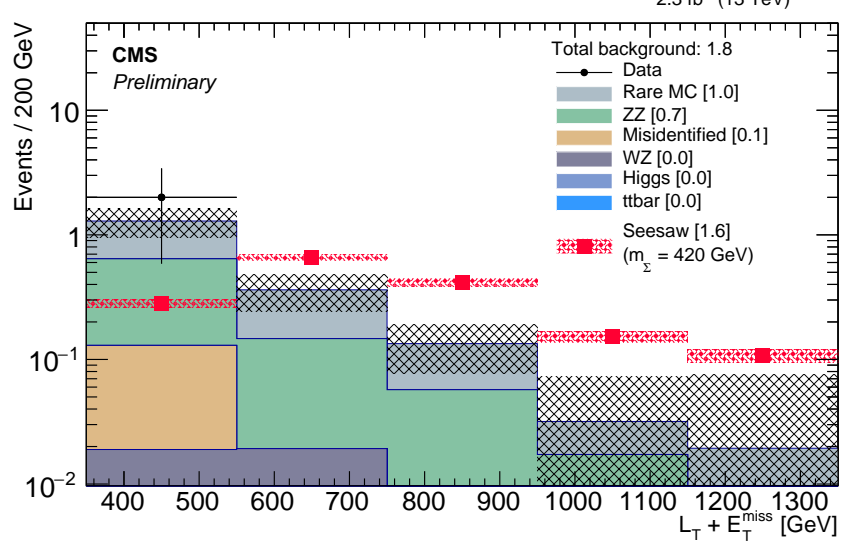
(a) 3 leptons with OSSF pair on-Z



(b) 3 leptons with OSSF pair above-Z

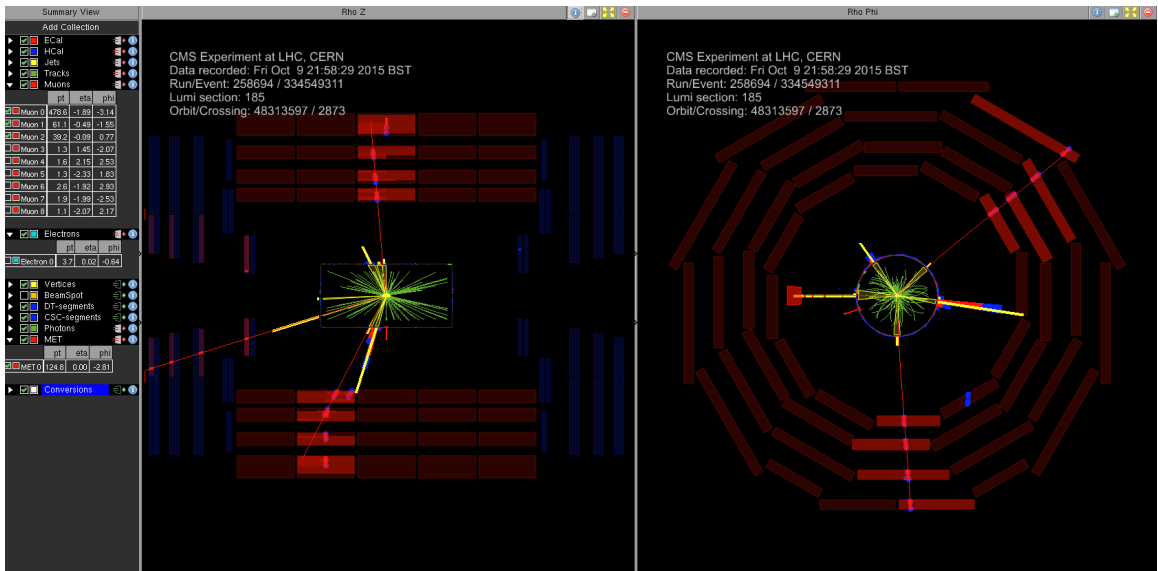


(c) 3 leptons, no OSSF pair

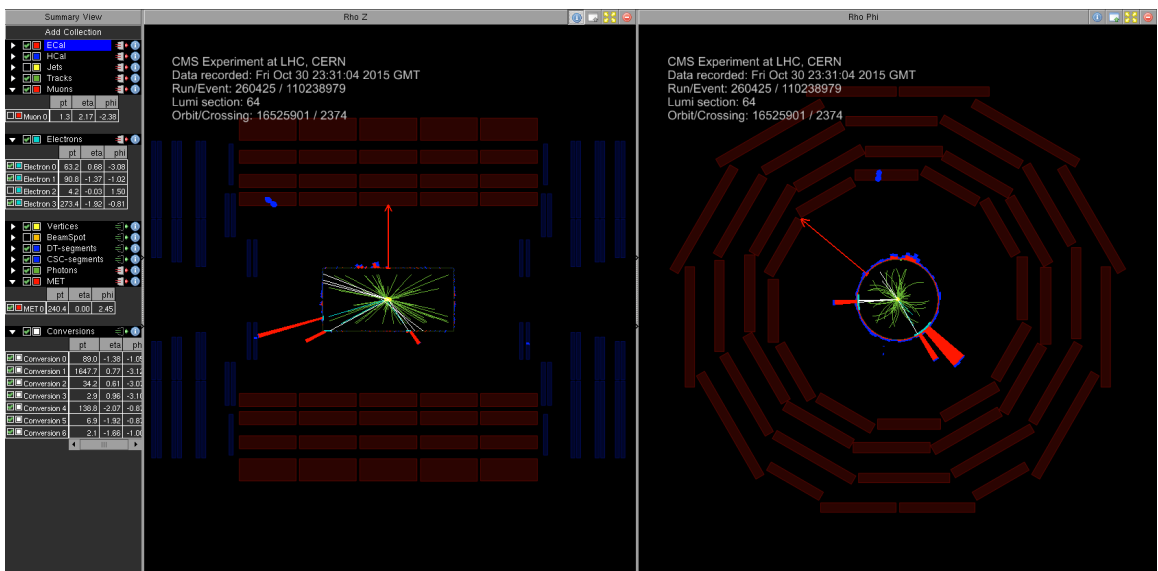


(d) 4 leptons, at least 1 OSSF pair

Figure 9.1: Results: $L_T + E_T^{\text{miss}}$ distributions (last bin includes overflow in all plots).



(a) DoubleMuon-triggered event



(b) DoubleEG-triggered event

Figure 9.2: Event displays for events from Fig. 9.1a.

Table 9.1: Relative Sensitivity of Signal Regions.

n_{leptons}	OSSF pair	$L_T + E_T^{\text{miss}}$ [GeV]	r_{exp}
3	above-Z	550–750	2.6953
3	none	550–750	3.6094
3	above-Z	750–950	4.0781
≥ 4	n/a	550–750	4.1094
≥ 4	n/a	750–950	5.5938
3	none	750–950	5.8750
3	above-Z	350–550	6.2500
3	on-Z	550–750	6.7188
3	none	350–550	7.5938
3	above-Z	950–1150	8.7812

9.2 Interpretation for the Seesaw Model

As no statistically significant excess was observed, we calculate expected and observed upper limits on the cross section sum for the production of seesaw heavy fermion pairs ($\Sigma^0\Sigma^+$, $\Sigma^0\Sigma^-$, or $\Sigma^+\Sigma^-$), assuming a flavor-democratic value for the mixing angle parameters, $V_e = V_\mu = V_\tau = 10^{-6}$, and degenerate heavy fermion masses m_Σ .

By comparing with the signal production cross section, one can translate the cross section limits into limits on the heavy fermion mass which can be excluded based on the data. In particular, taking r to be the ratio of the cross section limit and the signal production cross section, we can exclude the signal hypothesis when $r < 1$. The calculation is done using asymptotic CL_s limits with a confidence level of 95 % [50, 51, 52].

9.2.1 Single-channel Limits

We first compute limits for the 10 most sensitive of the bins displayed in Fig. 9.1. To get a feeling on how different signal regions contribute to the limits presented in Sec. 9.2, we present the expected single-channel r -values for these top 10 channels in Table 9.1, using the signal hypothesis with $m_\Sigma = 420 \text{ GeV}$.

As can be seen from the table, no single signal bin is sensitive enough to exclude the signal hypothesis; still, the table presents the relative sensitivities. However, we show below

that the combination of several of these channels is sensitive enough to exclude a considerable range of the signal mass parameter.

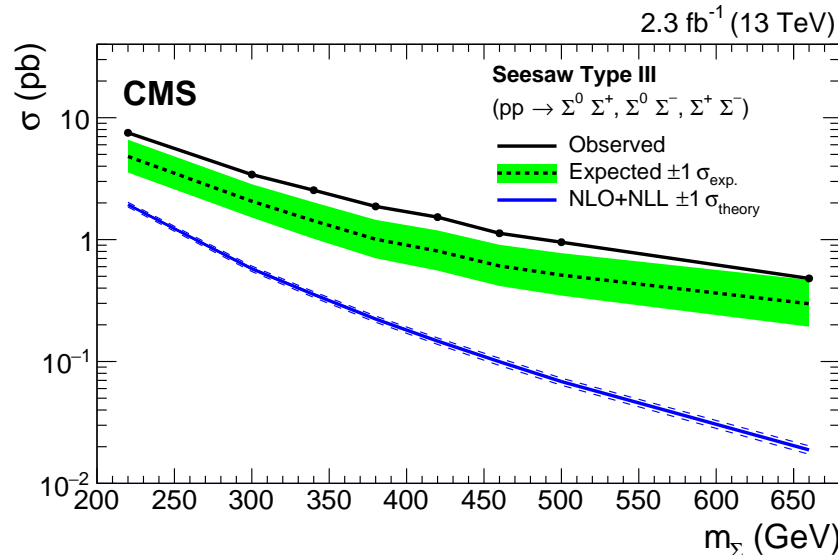
9.2.2 Multi-channel Limits

Fig. 9.3 shows the mass limits for each of the categories presented in Fig. 9.1. It can be seen that the observed limit is better, i.e. lower, than the expected limit whenever there is a deficiency observed in data. Similarly, when the data is high, the observed limit is worse than expected. This is the case in particular for the observed limit in Fig. 9.3a, as there is an excess of events in the corresponding signal region (Fig. 9.1a). However, the impact of this excess on the overall result is limited, as this particular signal region is not very sensitive to the type-III seesaw signal and thus yields cross section limits that are much higher than those of the other signal regions limits (see also Sec. 9.2.1). This can also be seen by the fact that this signal region is the only one that is not sensitive enough to exclude any of the masses probed, while the other signal regions achieve mass limits between 300 and 380 GeV on their own. (Masses to the left of the intersection point are excluded.)

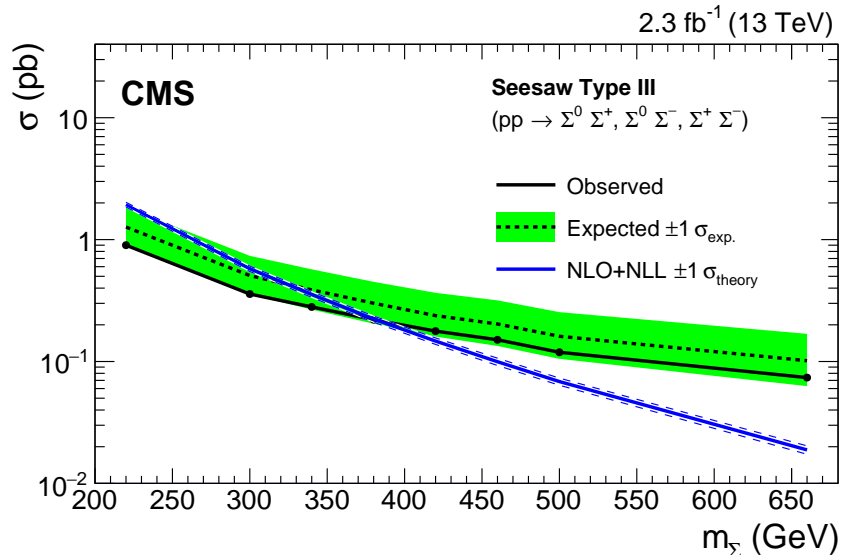
9.2.3 Full Combination

If the data agreed perfectly with the background estimates in all signal regions combined, we would expect our analysis to exclude type-III seesaw heavy fermion pair production for masses below $m_\Sigma = 430$ GeV. The combined observed limit is at 440 GeV. The full exclusion curve is shown in Fig. 9.4.

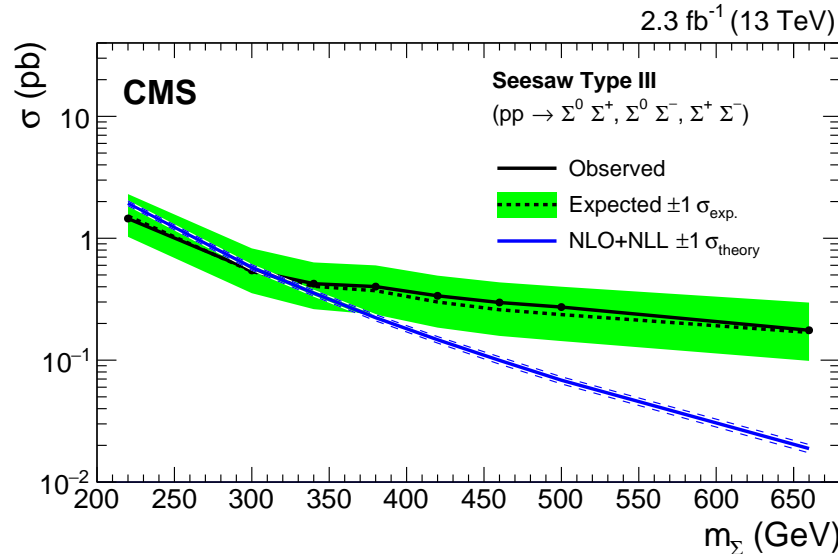
In comparison to the Run-I results, the search sensitivity has been enhanced by various improvements, most notably the inclusion of new decay modes involving the Higgs boson and of 4-lepton channels, as well as by the introduction of an improved fine-grained binning scheme. Exclusion limits from the CMS Run I result were at $m_\Sigma = 250$ GeV (expected) and $m_\Sigma = 278$ GeV (observed) [15].



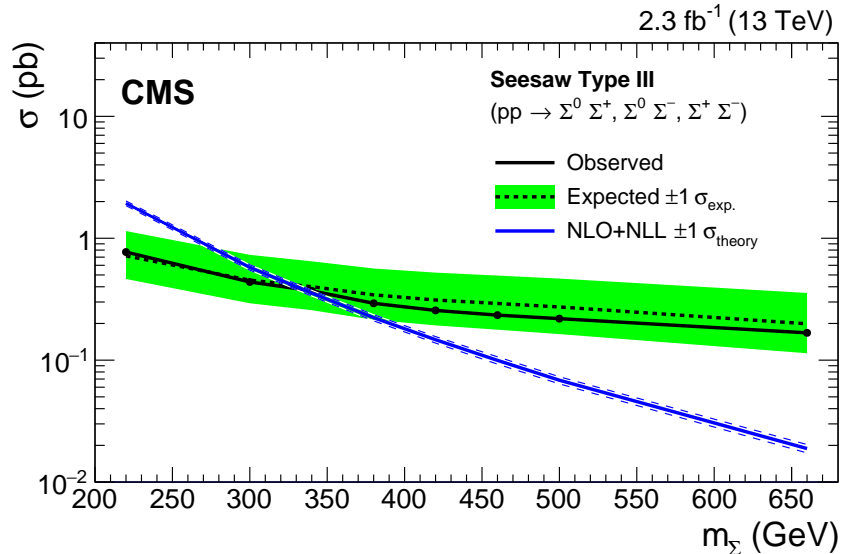
(a) 3 leptons with OSSF pair on-Z



(b) 3 leptons with OSSF pair above-Z



(c) 3 leptons, no OSSF pair



(d) 4 leptons, at least 1 OSSF pair

Figure 9.3: Results: Exclusion curves. Masses to the left of the intersection point are excluded.

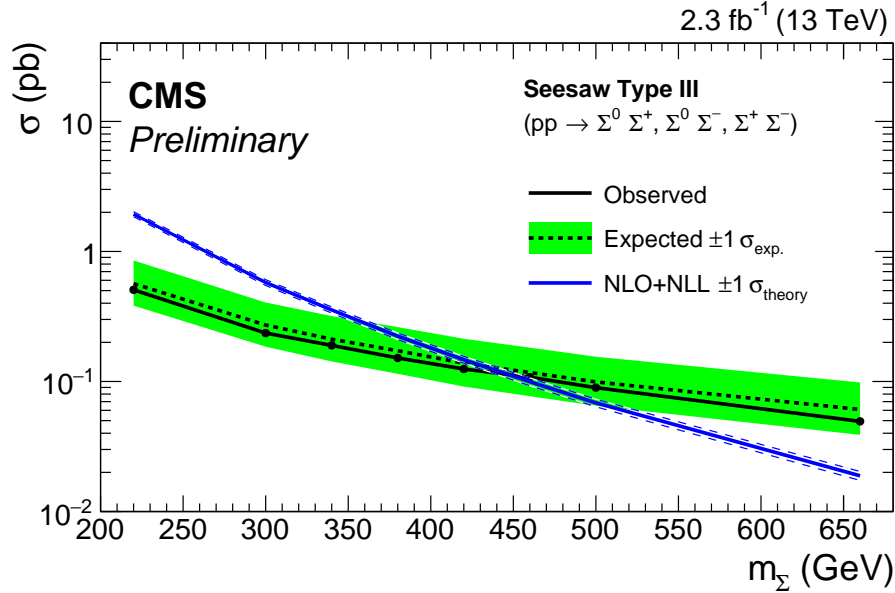


Figure 9.4: Exclusion for the flavor-democratic type-III seesaw model ($V_e = V_\mu = V_\tau = 10^{-6}$). We exclude heavy fermion pair production for masses below $m_\Sigma = 440$ GeV (expected: 430 GeV) and give upper limits on the pair production cross section.

9.3 Cross-checks

9.3.1 Back-of-the-Envelope Limits

We derive a rough estimate of the r -values for the $m_\Sigma = 220$ GeV mass point manually to verify that our result from Sec. 9.2 is in the right ballpark. The relatively low mass was chosen so that we obtain a sizeable number of expected signal events. We consider 4 groups of processes:

- $(\Sigma^\pm, \Sigma^0) \rightarrow (W^\pm \nu, W^\pm \ell^\mp)$
- $(\Sigma^\pm, \Sigma^0) \rightarrow (Z \ell^\pm, W^\pm \ell^\mp)$
- $(\Sigma^\pm, \Sigma^0) \rightarrow (H \ell^\pm, W^\pm \ell^\mp)$
- $(\Sigma^+, \Sigma^-) \rightarrow (Z \ell^+, Z \ell^-)$

These are the production and decay modes amongst the 27 combinations described in Sec. 2.3.1 that have the highest branching ratios to trilepton final states. Note that in the

Table 9.2: Most significant trilepton processes with branching ratios to the bosonic level.

Process	$\sigma \cdot \text{BR}$ [fb]	$N = \sigma \cdot \text{BR} \cdot \mathcal{L}$
$(\Sigma^\pm, \Sigma^0) \rightarrow (W^\pm \nu, W^\pm \ell^\mp)$	418	961
$(\Sigma^\pm, \Sigma^0) \rightarrow (Z \ell^\pm, W^\pm \ell^\mp)$	202	465
$(\Sigma^\pm, \Sigma^0) \rightarrow (H \ell^\pm, W^\pm \ell^\mp)$	100	230
$(\Sigma^+, \Sigma^-) \rightarrow (Z \ell^+, Z \ell^-)$	49	113

first three cases, we sum over the heavy fermion charges, so that the above list covers seven of the 27 processes.

We first estimate the expected number of decays from each of these processes, based on which we calculate how many of these events we expect to reconstruct and select in our analysis. We then compute back-of-the-envelope limits for a simplified search channel with exactly three light leptons¹.

To calculate the expected number of decays to the bosonic level from the most significant processes, we compute the product of the cross section and branching ratio for each process and then multiply by the luminosity (2.3 fb^{-1}) as shown in Table 9.2.

To obtain the expected number of reconstructed signal events, the number of expected decays then needs to be multiplied by the branching fractions from the bosonic to the leptonic level. We use $\text{BR}(W \rightarrow e \text{ or } \mu) = 23\%$, $\text{BR}(Z \rightarrow e \text{ or } \mu) = 16\%$, as well as $\text{BR}(\ell \rightarrow e \text{ or } \mu) = 72\%$ to take leptonic τ decays into account. Whenever a W boson is present, it has a much higher leptonic branching ratio than the Higgs or Z bosons which may also be present. Furthermore, there are two prompt leptons from the heavy fermion decay. In the presence of a W boson, we therefore ignore any Higgs and Z bosons for simplicity. The electron and muon reconstruction efficiency is taken at $\epsilon_{\text{lep}} = 83\%$. Table 9.3 shows the event yields with these branching ratios and efficiencies taken into account. As can be seen in the table, a total of about 74 signal events is expected.

We now consider the total background for three light leptons, only applying the lepton p_T thresholds (see Sec. 5.2) and the AIC veto. We find about 2000 events, based on which

¹We apply an AIC veto to reject events with an OSSF pair below Z when the trilepton invariant mass is on Z (see Sec. 7.3.2).

Table 9.3: Estimate of reconstructed trilepton signal events. The combined leptonic branching ratio of all involved bosons is denoted as BR_{lep} .

Process	$N \cdot \text{BR}_{\text{lep}}$	$N \cdot \text{BR}_{\text{lep}} \cdot \epsilon_{\text{lep}}^3$	Exact yield from full analysis
$(\Sigma^\pm, \Sigma^0) \rightarrow (W^\pm \nu, W^\pm \ell^\mp)$	36.6	20.9	13.9
$(\Sigma^\pm, \Sigma^0) \rightarrow (Z \ell^\pm, W^\pm \ell^\mp)$	55.4	31.7	35.9
$(\Sigma^\pm, \Sigma^0) \rightarrow (H \ell^\pm, W^\pm \ell^\mp)$	27.4	15.7	19.2
$(\Sigma^+, \Sigma^-) \rightarrow (Z \ell^+, Z \ell^-)$	9.4	5.4	5.7
Sum	128.8	73.7	74.7

we can set a 95 % C. L. limit of about $3 \cdot \sqrt{2000} \approx 134$ events. Relating this to the expected signal yields $r = \frac{74}{134} = 0.55$.

This number is larger by a factor of 1.9 than our main result at 220 GeV, indicating that our estimate has less sensitivity. The reason for this is that we did not use any kinematic binning to separate the signal from the background. Thus, the limit is worse, as expected, but not vastly off.

9.3.2 Simplified Limits from Leading Production and Decay Modes

The seven signal production and decay modes considered in 9.3.1 are responsible for the bulk of the detectable signal yield. Other modes contribute little due to small branching ratios to multilepton final states. We study what the limit would be if we only used these seven modes, and present the corresponding exclusion plot in Fig. 9.5.

While this exclusion plot visually differs little from the main result (Fig. 9.4), the degradation of the cross section limit value at 400 GeV is still 25 %, worsening the expected mass limit by about 45 GeV. This indicates that although the remaining 22 modes are of secondary importance, they should not be fully ignored.

9.3.3 Comparison to Run-I Results

We show that the sensitivity of our current analysis is plausible, given the improvements that were made in comparison to the Run I analysis [15]. To this end, we compute expected limits starting from a mock-up analysis setup that is very similar to the Run I analysis.

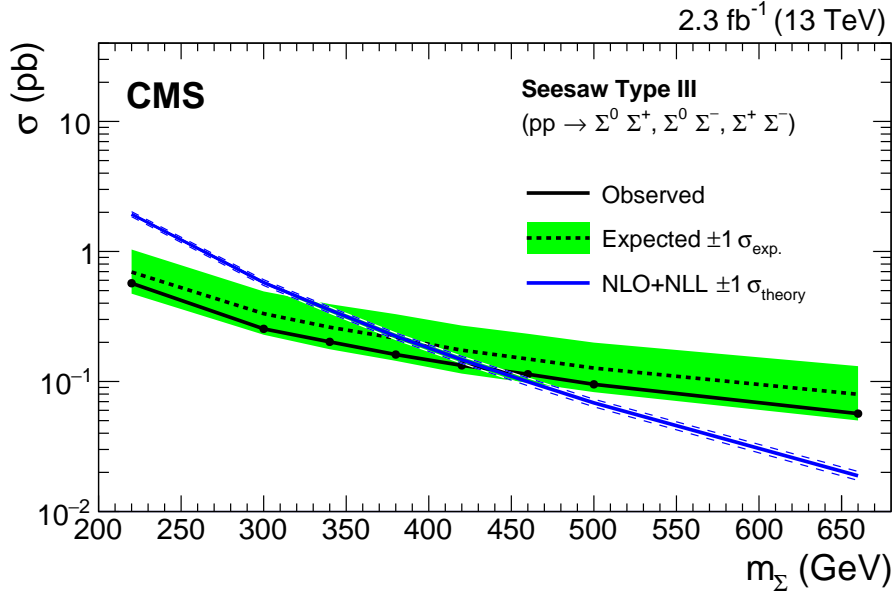


Figure 9.5: Exclusion for the flavor-democratic type-III seesaw model using the seven leading signal production/decay modes only.

As we then add various improvements, we arrive at the limit shown in Section 9.2. The investigations are done using the highest signal mass point considered in the Run I analysis ($m_\Sigma = 340$ GeV) and described in the following; a summary is presented in Table 9.4.

We extract the Run I expected r -value from Figure 2 in [15]. We find $\frac{\sigma_{\text{experimental}} \cdot \text{BR}}{\sigma_{\text{theory}} \cdot \text{BR}} = \frac{14}{4.3} \text{fb} = 3.26$. To relate this 8 TeV number to the current 13 TeV dataset with 2.3 fb^{-1} , we divide the r -value by the cross-section ratio $\frac{\sigma(13 \text{ TeV})}{\sigma(8 \text{ TeV})} = 3.10$ and multiply by a correction factor for the different luminosities, $\sqrt{19.5/2.3}$. We thus find that the Run I analysis sensitivity corresponds to an expected r -value of $r_{\text{exp}} = 3.06$ at 13 TeV.

Using a mock-up Run I analysis setup based on charge binning with the 13 TeV dataset (2.3 fb^{-1}), we actually find an expected r -value of $r_{\text{exp}} = 4.11$ (exactly 3 electrons or muons, p_T thresholds at 30/20/20 GeV, $E_T^{\text{miss}} > 50$ GeV, $H_T < 150$ GeV, Z veto, AIC veto). The two charge bins that this limit is based on are displayed in Fig. 9.6.

4.11 is worse than 3.06 by 34 % which is roughly the size of the uncertainty. Furthermore, the various approximations we made to mimic the Run I analysis may cause such a difference.

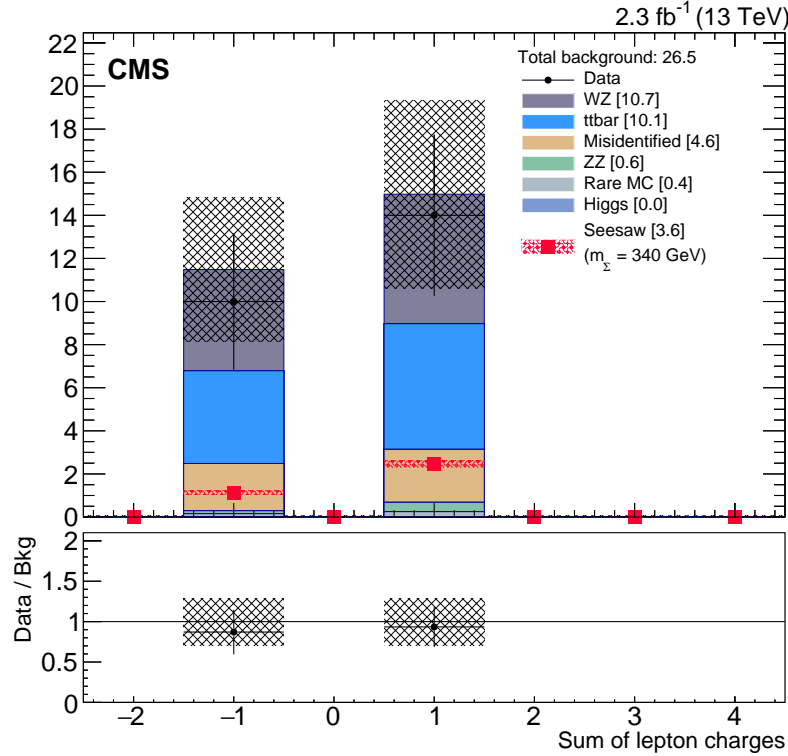


Figure 9.6: Bins of lepton charge sum used in mock-up Run I result, with 13 TeV dataset and background estimates (3 leptons only).

Also, the Run I analysis used somewhat finer flavor-dependent binning scheme. In any case, the discrepancy is in the conservative direction.

Now, starting from $r_{\text{exp}} = 4.11$, we show how various improvements lead to the r -value of 0.60 which is presented in Section 9.2. Table 9.4 shows the details of how the limits improve.

Table 9.4: Sensitivity improvements compared to the Run I analysis.

r_{exp}	Gain	Step
3.26		Run I result
3.06		Run I result translated to 2.3 fb^{-1} at 13 TeV
4.11	–	Run I result with Run I mock-up analysis setup
1.96	52 %	mock-up analysis with current p_T thresholds and kinematic cuts
1.19	39 %	adding signal with Higgs decay modes
0.78	34 %	switching to $L_T + E_T^{\text{miss}}$ binning (= current search with only 3 leptons)
0.60	23 %	adding 4-lepton channels (= current result)

Chapter 10

Conclusion

A search for type-III seesaw heavy fermion production has been performed in multilepton final states using 2.3 fb^{-1} of proton–proton collision data at $\sqrt{s} = 13 \text{ TeV}$, collected using the CMS detector at the CERN LHC. No significant discrepancies between the background prediction and the data have been observed. Comparing the data with the predictions, we set upper limits at the 95 % confidence level on the production cross section of the heavy fermion pairs. Assuming degenerate heavy fermion masses m_Σ in the flavor-democratic scenario, we exclude previously unexplored regions of the signal model with heavy fermion particle masses below $m_\Sigma < 440 \text{ GeV}$ (expected: 430 GeV).

Appendix A

Suitability of Tracks as Fake Proxies

We look at the invariant mass of opposite-sign muon + track pairs. If the tracks are uncorrelated with the muons, we expect a broad peak at the average invariant mass. If they are correlated, they will be related to their source, for example a Z decay. In fact, we see both (Figure A.1).

This suggests that tracks are not only from jets, but also from low quality leptons. So, tracks do model fake leptons from jets, and at the same time also model leptons that were vetoed by quality cuts. However, since both effects also occur in the signal regions, the overall shape of the track background is still expected to be accurate there.

Note that the numbers in Fig. A.1 have been derived with the 8 TeV CMS dataset from Run I. The conclusions, however, are also valid for Run II at 13 TeV.

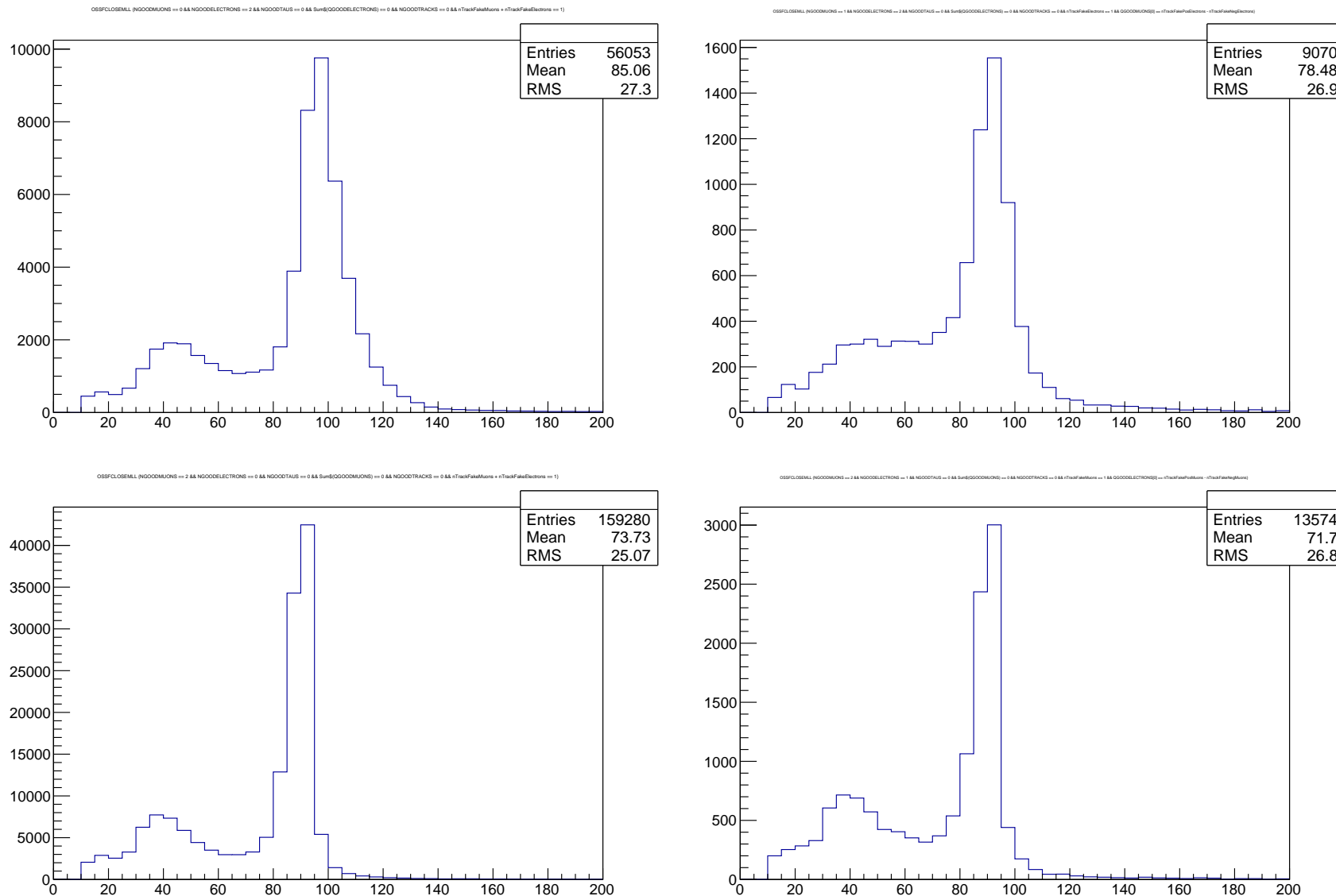


Figure A.1: Top: m_{et} distribution; bottom: m_{μ} distribution. Left: no other leptons present, right: additional lepton present. If a third lepton is present, its flavor is opposite of the first lepton, and its charge is the same as the track's (rejecting third leptons from Z).
Note: This is from the dilepton-triggered dataset, i.e. the tracks used here probably were good enough leptons to trigger.

Appendix B

Analysis Software

The analysis conducted in this thesis requires processing large amounts of data, both as additional datasets arrive from CERN, and also repeatedly as analysis needs develop. It is thus crucial that the software used to process the data performs efficiently, allowing the analysis to progress rapidly without much computational delay. To achieve this, our research group has developed a three-tier C++ ecosystem, based on standard CERN software.

B.1 RutgersAODReader

The CMS experiment provides measurement data and simulated samples in the so-called MiniAOD format. This format can be decoded using the CMSSW software [53] which is built on top of the ROOT data analysis framework [54].

RutgersAODReader interfaces with CMSSW to extract event information from measurement data and simulated samples which is then used to create simple collections of objects that are associated with particles reconstructed by the detector. Those collections, also called “products”, are stored along with a few basic analysis variables like E_T^{miss} in so-called flat ntuple files using the standard ROOT file format.

B.2 EventAnalyzer

EventAnalyzer uses RutgersAODReader’s flat ntuple output files as input. It then proceeds with higher-level computations, such as calculating isolation and other object-specific variables (see Sec. 5.1), and creating collections of reconstructed particles with additional

RutgersIAF EventAnalyzer Objects

Matrix Method	Common	RA7
looseMatrixMuons tightMatrixMuons	goodMuons goodElectrons goodTaus goodJets goodForwardJets goodbJetsCSV goodbJetsCSVM	looseMatrixMuons foRA7Muons tightRA7Muons
looseMatrixElectrons tightMatrixElectrons heepIDElectrons	goodPhotons goodTracks	looseMatrixElectrons foRA7Electrons tightRA7Electrons
looseMatrixTaus tightMatrixTaus		tightRA7Taus* <small>*not included in DR cleaning</small>
matrixJets matrixForwardJets matrixbJetsCSV matrixbJetsCSVM	basicMuons basicElectrons basicTaus basicJets basicPhotons basicTracks	RA7Jets RA7ForwardJets RA7bJetsCSV RA7bJetsCSVM
+DR arbitration	recoVertices recoVerticesDrCleaned hltJets	+DR arbitration

Figure B.1: Overview of the object collections used in EventAnalyzer.

selection criteria such as collections of “good muons” and “good electrons” which fulfill the analysis requirements (isolation, promptness, etc.). The software also provides capabilities to make sure that objects do not overlap; for example, one can discard electrons that are too close to a reconstructed muon. Furthermore, particles can be reassigned to collections of another type, as is needed for the implementation of our fake rate method (see Sec. 7.3.1).

Fig. B.1 displays an overview of the various collections used.

After calculating all “object variables”, additional “event variables” are computed. While those may be constructed from object variables, they do not pertain to a specific reconstructed particle, but always represent properties of the event as a whole. Just like object variables, they can be of various data types. Examples are the number of leptons passing all quality requirements (integer), the scalar sum L_T of lepton transverse momenta (float), or a boolean

specifying whether an event contains an OSSF lepton pair whose invariant mass is consistent with a Z boson decay (see Chapter 6). The categorization of data, background, and signal events into control regions and signal regions is usually based on such event variables.

EventAnalyzer provides several output mechanisms, from condensed histograms to full event dumps. In most cases, the so-called AnalysisTree output format is used. It is based on the standard ROOT file format and contains all computed event variables in a way that is easily accessible subsequently, either directly from the ROOT command prompt, or from within additional software that reads AnalysisTree files. Special storage mechanisms for boolean event variables and certain event weights are, however, incompatible with standard ROOT tools such as `hadd` (used for combining multiple files) and require custom variants of these tools (specifically, `haddR`).

All of EventAnalyzer’s actions are configured through a configuration file. While the EventAnalyzer engine itself is agnostic of the specific type of physics that is being investigated, it understands concepts such as particle collections, momentum vectors, spatial distance, or invariant mass. The configuration file is used to specify which particles are to be related in which ways, how particle collections are to be formed, and which event variables are to be calculated and stored in the output file for later use. It also allows specifying the output format as well as skimming criteria in order to save on storage and processing time.

B.3 AnalysisPresenter

B.3.1 Scope and Design Principles

Once all data, background, and signal samples have been made available in AnalysisTree format, AnalysisPresenter is used to categorize events, apply event weights (such as pile-up, p_T , or n_{jets} corrections), estimate the data-driven fake backgrounds by applying fake rates (including any parameterizations that may have been defined) to the seed samples (see Sec. 7.3), and scale MC backgrounds and signal to the data luminosity.

These scalings are performed on the fly at the time of reading events from the AnalysisTree input files. For each sample that is read in, a multidimensional histogram is created in memory which is filled using weights as prescribed by the scalings. Just like EventAnalyzer, the AnalysisPresenter engine is unaware of the physics that is being considered. Instead, the user needs to specify the variables of interest and the binning scheme through a configuration file. The axes of the multidimensional histogram are constructed based on these specifications and can later be used for cutting and binning. An axis can either be any event variable stored in the AnalysisTree, or a combination thereof. Simple combinations can be declared inline, while more complicated functions (such as a hash of the event number) require resorting to a user-defined C++ function from within the axis specification. Statistical uncertainties are stored with each bin that is populated.

AnalysisPresenter also allows modeling systematic uncertainties for backgrounds and signal. Correlations and anti-correlations can be modeled both between samples (e.g. the luminosity uncertainty for rare backgrounds estimated from MC, and for signal) as well as between bins within the same sample (e.g. bin migration due to E_T^{miss} uncertainties). To keep track of these details for every sample, a copy of the multidimensional histogram is filled for each systematic uncertainty and sample, with a variation by one standard deviation applied. By subtracting the nominal histogram, the absolute impact of the systematic uncertainty can be determined; the sign distinguishes anti-correlations from correlations. Systematic uncertainties are specified either as a percentage number, as a formula that depends on arbitrary event variables or user-defined functions, or by declaring that an event variable be replaced by another one in order to evaluate the changes in how the multidimensional histogram is populated.

B.3.2 Distributions

Simple distributions like the $L_T + E_T^{\text{miss}}$ distributions in Fig. 6.2 can be made in a straightforward manner from the multidimensional histograms: First, cuts are applied by setting an

“axis range”, such as $3 \leq n_{\text{leptons}} \leq 4$ to require three or four leptons. This can be thought of as slicing out a subset from the multidimensional histogram. Second, a projection is taken onto the axis of interest, e.g. $L_T + E_T^{\text{miss}}$. When projecting, the histogram is collapsed into a one-dimensional histogram along the projection axis; bins along all other dimensions are integrated. Statistical uncertainties are added in quadrature; systematic uncertainties are taken care of by repeating the slicing and projection steps with the corresponding copies of the multidimensional histograms.

The projection method returns a C++ object that offers various ways to output the resulting distributions, for example as a plot like in Fig. 6.2, or as a plain text table. Within each projection object, an event list is stored along with the data, background, and signal histograms. This allows for easy investigation of interesting events.

B.3.3 Bundling Mechanism and MC Subtraction

As described in Sec. 2.3.2, the signal consists of 27 different processes which we generate separately. It is desirable that those samples are summed up and displayed together. Similarly, one might want to combine several rare backgrounds into one, to avoid visual clutter. For this purpose, AnalysisPresenter supports the bundling of samples. The bundling is performed after cutting and projecting has been done.

The bundling mechanism may not only be used for presentation purposes, but also for physical purposes. Our fake rate method, for example, requires subtracting an overlapping prediction from the $t\bar{t}$ MC simulation. This can be handled by declaring the overlapping $t\bar{t}$ background estimate as an additional background process in the AnalysisPresenter configuration file, yet with a negative weight. This estimate can then be bundled with the fake background prediction itself; the negative weights for the $t\bar{t}$ component will effect the desired subtraction. The result is what’s labeled the “TrackFakes” component in Fig. 7.9.

Contributions of single processes share the same C++ interface as bundles of processes. This means that bundles may in turn be bundled up with other processes or bundles. For

example, the “Misidentified” component in Fig. 7.2 is a bundle of the “TrackFakes” and the “PhotonFakes” bundles. The summation is done for visual purposes only.

As we have seen, it is desirable to allow histogram bins to assume negative values for the purposes of MC subtraction through the bundling mechanism. Another use case of negative bin contents is when an MC generator such as MadGraph5_aMC@NLO [35] provides negative weights for some events. For bins in the tails of the multidimensional histograms, it may then happen that they are predominantly populated by events with negative weights. This is an artifact of the fact that the multidimensional histograms are extremely finely binned: Upon projection on any axis, the other axes are integrated over, so that the result will usually turn out positive. It is thus important to keep the negative bins in the multidimensional histogram; discarding them would bias the histogram integral to higher average values when the binning scheme is replaced by a more granular one. For this reason, the user may want to enforce only after projecting onto the axis of interest that any negative bin contents be replaced by zero, in order to make sure predictions are physical.

Thus, for each contribution (bundled or not), the user may specify whether bin contents should be bounded by 0 from below, depending on whether the contribution is intended to be used for subtraction purposes via the bundling mechanism or not.

B.3.4 Channel Collections and Datacards

A set of cuts (axis ranges) can be frozen into a “channel”. Channels share the same C++ interface as projections; in particular, they can be output as a plot or a table.

In addition, multiple channels can be combined into a structure called “channel collection”. From this structure, AnalysisPresenter can create a so-called datacard which contains information on observation, signal, and background composition of all the channels involved, as well as statistical and systematic uncertainties including their correlations. The datacard format is compatible with the standard CMS statistics tools and can be used for statistical interpretation of the analysis, as is done in Sec. 9.2.

When creating a datacard, the bundling prescriptions are observed. This is not only important for purposes of MC subtraction, but also useful to limit the level of detail in the datacard in order to reduce the runtime of the statistical interpretation (e.g. to combine rare backgrounds). Furthermore, it is enforced that the channels within a channel collection are exclusive, by requiring their event lists to be disjunct.

B.3.5 Runtime

AnalysisPresenter is mainly a categorization tool and does not actually calculate sophisticated physical quantities like invariant masses. (This is the task of EventAnalyzer, see Sec. B.2). It therefore can populate its main data structures—the multidimensional histograms—at a rate of about 20000 events per second. Nevertheless, the bulk of the processing time is due to reading events from the input files (between a few seconds and several minutes, depending on the size of the input).

Cuts, projections, bundlings, as well as channel collection and datacard creation are then performed within a fraction of second. Since it is possible to change the cuts at runtime, various types of output can be created for different selections without rereading the samples. Thus, if the user plans ahead and declares all axes that are intended to be used for cutting and binning, changes to the analysis selection can be studied very quickly in various regions. The runtime is roughly proportional to the number of samples and to the number of systematic uncertainties declared, and also depends on the binning granularity since the bookkeeping overhead increases with the number of bins.

Bibliography

- [1] P. Thomassen. “Search for Multi-Lepton Events from Strong and Electroweak SUSY Production in pp Collisions at $\sqrt{s} = 7$ TeV”. MA thesis. Rutgers, 2012.
- [2] *Search for Type-III Seesaw Heavy Fermions with Multilepton Final States using 2.3/fb of 13 TeV proton-proton Collision Data*. Tech. rep. CMS-PAS-EXO-16-002. Geneva: CERN, 2016. URL: <https://cds.cern.ch/record/2140978>.
- [3] I.J.R. Aitchison and A.J.G. Hey. *Gauge Theories in Particle Physics: Volume I: From Relativistic Quantum Mechanics to QED, Third Edition*. Gauge Theories in Particle Physics: A Practical Introduction. Taylor & Francis, 2003. ISBN: 9780750308649. URL: <https://books.google.ch/books?id=7cX8nQEACAAJ>.
- [4] I.J.R. Aitchison and A.J.G. Hey. *Gauge Theories in Particle Physics, Volume II: QCD and the Electroweak Theory, Third Edition*. Graduate Student Series in Physics. CRC Press, 2003. ISBN: 9780849387760. URL: <https://books.google.ch/books?id=-mDjFSUDQsEC>.
- [5] Michael E Peskin and Daniel V Schroeder. *An Introduction to Quantum Field Theory; 1995 ed.* Includes exercises. Boulder, CO: Westview, 1995. URL: <https://cds.cern.ch/record/257493>.
- [6] Lyndon Evans and Philip Bryant. “LHC Machine”. In: *JINST* 3 (2008), S08001. DOI: [10.1088/1748-0221/3/08/S08001](https://doi.org/10.1088/1748-0221/3/08/S08001).
- [7] K. A. Olive et al. “Review of Particle Physics”. In: *Chin. Phys. C* 38 (2014), p. 090001. DOI: [10.1088/1674-1137/38/9/090001](https://doi.org/10.1088/1674-1137/38/9/090001).
- [8] F. Capozzi et al. “Status of three-neutrino oscillation parameters, circa 2013”. In: *Phys. Rev. D* 89 (2014), p. 093018. eprint: [1312.2878](https://arxiv.org/abs/1312.2878).
- [9] R. Foot et al. “See-saw neutrino masses induced by a triplet of leptons”. In: *Z. Phys. C* 44 (1989). DOI: [10.1007/BF01415558](https://doi.org/10.1007/BF01415558).
- [10] S. Chatrchyan et al. “The CMS experiment at the CERN LHC”. In: *JINST* 3 (2008), S08004. DOI: [10.1088/1748-0221/3/08/S08004](https://doi.org/10.1088/1748-0221/3/08/S08004).
- [11] Serguei Chatrchyan et al. “Search for top squarks in R -parity-violating supersymmetry using three or more leptons and b-tagged jets”. In: *Phys. Rev. Lett.* 111.22 (2013), p. 221801. DOI: [10.1103/PhysRevLett.111.221801](https://doi.org/10.1103/PhysRevLett.111.221801). arXiv: [1306.6643 \[hep-ex\]](https://arxiv.org/abs/1306.6643).
- [12] Serguei Chatrchyan et al. “Search for anomalous production of events with three or more leptons in pp collisions at $\sqrt(s) = 8$ TeV”. In: *Phys. Rev. D* 90 (2014), p. 032006. DOI: [10.1103/PhysRevD.90.032006](https://doi.org/10.1103/PhysRevD.90.032006). arXiv: [1404.5801 \[hep-ex\]](https://arxiv.org/abs/1404.5801).
- [13] Vardan Khachatryan et al. “Searches for electroweak neutralino and chargino production in channels with Higgs, Z, and W bosons in pp collisions at 8 TeV”. In: *Phys. Rev. D* 90.9 (2014), p. 092007. DOI: [10.1103/PhysRevD.90.092007](https://doi.org/10.1103/PhysRevD.90.092007). arXiv: [1409.3168 \[hep-ex\]](https://arxiv.org/abs/1409.3168).

- [14] Vardan Khachatryan et al. “Searches for heavy Higgs bosons in two-Higgs-doublet models and for $t \rightarrow ch$ decay using multilepton and diphoton final states in pp collisions at 8 TeV”. In: *Phys. Rev.* D90 (2014), p. 112013. doi: [10.1103/PhysRevD.90.112013](https://doi.org/10.1103/PhysRevD.90.112013). arXiv: [1410.2751 \[hep-ex\]](https://arxiv.org/abs/1410.2751).
- [15] *Search for heavy lepton partners of neutrinos in pp collisions at 8 TeV, in the context of type III seesaw mechanism*. Tech. rep. CMS-PAS-EXO-14-001. Geneva: CERN, 2015. URL: <http://cds.cern.ch/record/2000982>.
- [16] “Search for type-III Seesaw heavy leptons in pp collisions at 8 TeV with the ATLAS Detector”. In: *Phys. Lett. D* 92 (2015), p. 032001. doi: [10.1103/PhysRevD.92.032001](https://doi.org/10.1103/PhysRevD.92.032001). eprint: [1506.01839](https://arxiv.org/abs/1506.01839).
- [17] “Search for heavy lepton partners of neutrinos in proton-proton collisions in the context of the type III seesaw mechanism”. In: *Phys. Lett. D* 718 (2012), p. 348. doi: [10.1016/j.physletb.2012.10.070](https://doi.org/10.1016/j.physletb.2012.10.070). eprint: [1210.1797](https://arxiv.org/abs/1210.1797).
- [18] “First combination of Tevatron and LHC measurements of the top-quark mass”. In: (2014). arXiv: [1403.4427 \[hep-ex\]](https://arxiv.org/abs/1403.4427).
- [19] Georges Aad et al. “Combined Measurement of the Higgs Boson Mass in pp Collisions at $\sqrt{s} = 7$ and 8 TeV with the ATLAS and CMS Experiments”. In: *Phys. Rev. Lett.* 114 (2015), p. 191803. doi: [10.1103/PhysRevLett.114.191803](https://doi.org/10.1103/PhysRevLett.114.191803). arXiv: [1503.07589 \[hep-ex\]](https://arxiv.org/abs/1503.07589).
- [20] A. Pomarol. “Beyond the Standard Model”. In: *High-energy Physics. Proceedings, 18th European School, ESHEP 2010, Raseborg, Finland, 20 Jun. - 3 Jul., 2010*. 2012, pp. 115–151. arXiv: [1202.1391 \[hep-ph\]](https://arxiv.org/abs/1202.1391). URL: <https://inspirehep.net/record/1088246/files/arXiv:1202.1391.pdf>.
- [21] Stephen P. Martin. “A Supersymmetry primer”. In: *Adv. Ser. Direct. High Energy Phys.* 21 (2010), p. 1. doi: [10.1142/9789814307505_0001](https://doi.org/10.1142/9789814307505_0001). arXiv: [hep-ph/9709356v6 \[hep-ph\]](https://arxiv.org/abs/hep-ph/9709356v6).
- [22] J. Schechter and J. W. F. Valle. “Neutrino masses in $SU(2) \otimes U(1)$ theories”. In: *Phys. Rev. D* 22 (9 1980), pp. 2227–2235. doi: [10.1103/PhysRevD.22.2227](https://doi.org/10.1103/PhysRevD.22.2227). URL: <http://link.aps.org/doi/10.1103/PhysRevD.22.2227>.
- [23] Y. Fukuda et al. “Measurements of the solar neutrino flux from Super-Kamiokande’s first 300 days”. In: *Phys. Rev. Lett.* 81 (1998). [Erratum: *Phys. Rev. Lett.* 81,4279(1998)], pp. 1158–1162. doi: [10.1103/PhysRevLett.81.1158](https://doi.org/10.1103/PhysRevLett.81.1158). arXiv: [hep-ex/9805021 \[hep-ex\]](https://arxiv.org/abs/hep-ex/9805021).
- [24] T. Han and B. Zhang. “Signatures for Majorana neutrinos at hadron colliders”. In: *Phys. Rev. Lett.* 97 (2006). doi: [10.1103/PhysRevLett.97.171804](https://doi.org/10.1103/PhysRevLett.97.171804). eprint: [hep-ph/0604064](https://arxiv.org/abs/hep-ph/0604064).
- [25] P. Minkowski. “ $\mu \rightarrow e\gamma$ at a rate of one out of 10^9 muon decays?” In: *Phys. Lett. B* 67 (1977), p. 421. doi: [10.1016/0370-2693\(77\)90435-X](https://doi.org/10.1016/0370-2693(77)90435-X).
- [26] R.N. Mohapatra, N. Rabindra, and G. Senjanovic. “Neutrino Mass and Spontaneous Parity Violation”. In: *Phys. Rev. Lett.* 44 (1980), p. 912. doi: [10.1103/PhysRevLett.44.912](https://doi.org/10.1103/PhysRevLett.44.912).
- [27] T. Yanagida. “Neutrino Mass in seesaw type I”. In: *Proc. of the Workshop on Unified Theory and Baryon Number of the Universe* 64 (1979), p. 1103.

- [28] M. Magg and C. Wetterich. “Neutrino Mass Problem and Gauge Hierarchy”. In: *Phys. Rev. B* 94 (1980), p. 61. DOI: [10.1016/0370-2693\(80\)90825-4](https://doi.org/10.1016/0370-2693(80)90825-4).
- [29] J. Schechter and J. Valle. “Neutrino masses in SU(2)xU(1) theories”. In: *Phys. Rev. D* 22 (1980), p. 2227. DOI: [10.1103/PhysRevD.22.2227](https://doi.org/10.1103/PhysRevD.22.2227).
- [30] C. Wetterich. “Neutrino Masses and the Scale of B-L Violation”. In: *Nucl. Phys. B* 187 (1981), p. 343. DOI: [10.1016/0550-3213\(81\)90279-0](https://doi.org/10.1016/0550-3213(81)90279-0).
- [31] G. Lazarides, Q. Shafi, and C. Wetterich. “Proton Lifetime and Fermion Masses in an SO(10) Model”. In: *Nucl. Phys. B* 181 (1981), p. 287. DOI: [10.1016/0550-3213\(81\)90354-0](https://doi.org/10.1016/0550-3213(81)90354-0).
- [32] R.N. Mohapatra and G. Senjanovic. “Neutrino Masses and Mixings in Gauge Models with Spontaneous Parity Violation”. In: *Phys. Rev. D* 23 (1981), p. 165. DOI: [10.1103/PhysRevD.23.165](https://doi.org/10.1103/PhysRevD.23.165).
- [33] M.C. Gonzalez-Garcia and J. Valle. “Fast decaying neutrinos and observable flavor violation in a new class of Majoron models”. In: *Phys. Lett. B* 216 (1989), p. 360. DOI: [10.1016/0370-2693\(89\)91131-3](https://doi.org/10.1016/0370-2693(89)91131-3).
- [34] C. Biggio and F. Bonnet. “Implementation of the type III seesaw model in FeynRules/MadGraph and prospects for discovery with early LHC data”. In: *Eur. Phys. J. C* 72 (2012), p. 1899. DOI: [10.1140/epjc/s10052-012-1899-z](https://doi.org/10.1140/epjc/s10052-012-1899-z). eprint: [1107.3463v3](https://arxiv.org/abs/1107.3463v3).
- [35] J. Alwall et al. “The automated computation of tree-level and next-to-leading order differential cross sections, and their matching to parton shower simulations”. In: *JHEP* 07 (2014), p. 079. DOI: [10.1007/JHEP07\(2014\)079](https://doi.org/10.1007/JHEP07(2014)079). arXiv: [1405.0301 \[hep-ph\]](https://arxiv.org/abs/1405.0301).
- [36] Torbjorn Sjöstrand, Stephen Mrenna, and Peter Z. Skands. “A Brief Introduction to PYTHIA 8.1”. In: *Comput. Phys. Commun.* 178 (2008), pp. 852–867. DOI: [10.1016/j.cpc.2008.01.036](https://doi.org/10.1016/j.cpc.2008.01.036). arXiv: [0710.3820 \[hep-ph\]](https://arxiv.org/abs/0710.3820).
- [37] Benjamin Fuks et al. “Gaugino production in proton-proton collisions at a center-of-mass energy of 8 TeV”. In: *JHEP* 1210 (2012), p. 081. DOI: [10.1007/JHEP10\(2012\)081](https://doi.org/10.1007/JHEP10(2012)081). arXiv: [1207.2159v2 \[hep-ph\]](https://arxiv.org/abs/1207.2159v2).
- [38] Benjamin Fuks et al. “Precision predictions for electroweak superpartner production at hadron colliders with Resummino”. In: *Eur. Phys. J. C* 73 (2013), p. 2480. DOI: [10.1140/epjc/s10052-013-2480-0](https://doi.org/10.1140/epjc/s10052-013-2480-0). arXiv: [1304.0790v2 \[hep-ph\]](https://arxiv.org/abs/1304.0790v2).
- [39] Lyndon Evans and Philip Bryant. “LHC Machine”. In: *Journal of Instrumentation* 3.08 (2008), S08001. URL: <http://stacks.iop.org/1748-0221/3/i=08/a=S08001>.
- [40] Christiane Lefèvre. “The CERN accelerator complex. Complexe des accélérateurs du CERN”. 2008. URL: <https://cds.cern.ch/record/1260465>.
- [41] Marzena Lapka. *Slice of the CMS detector*. 2011. URL: <https://cms-docdb.cern.ch/cgi-bin/PublicDocDB>ShowDocument?docid=4172> (visited on 03/22/2016).
- [42] Si Xie and C Paus. “Search for the Standard Model Higgs Boson Decaying to Two W Bosons at CMS”. Presented 07 May 2012. PhD thesis. MIT, 2012. URL: <https://cds.cern.ch/record/1455454>.
- [43] Eva Halkiadakis. “Introduction to the LHC Experiments”. In: *Physics of the large and the small, TASI 09, proceedings of the Theoretical Advanced Study Institute in Elementary Particle Physics, Boulder, Colorado, USA, 1-26 June 2009*. 2011, pp. 489–518. DOI: [10.1142/9789814327183_0009](https://doi.org/10.1142/9789814327183_0009). arXiv: [1004.5564 \[hep-ex\]](https://arxiv.org/abs/1004.5564). URL: <https://inspirehep.net/record/853601/files/arXiv:1004.5564.pdf>.

- [44] R. Bock and A. Vasilescu. *The Particle Detector BriefBook*. Accelerator Physics. Springer Berlin Heidelberg, 2013. ISBN: 9783662037270. URL: <https://books.google.fr/books?id=GS7qCAAAQBAJ>.
- [45] *Particle-Flow Event Reconstruction in CMS and Performance for Jets, Taus, and MET*. Tech. rep. CMS-PAS-PFT-09-001. 2009. Geneva: CERN, 2009. URL: <https://cds.cern.ch/record/1194487>.
- [46] *Search for SUSY in same-sign dilepton events at sqrt(s)=13 TeV*. Tech. rep. CMS-PAS-SUS-15-008. Geneva: CERN, 2015. URL: <https://cds.cern.ch/record/2114813>.
- [47] Keith Rehermann and Brock Tweedie. “Efficient Identification of Boosted Semileptonic Top Quarks at the LHC”. In: *JHEP* 03 (2011), p. 059. DOI: [10.1007/JHEP03\(2011\)059](https://doi.org/10.1007/JHEP03(2011)059). arXiv: [1007.2221 \[hep-ph\]](https://arxiv.org/abs/1007.2221).
- [48] *MET performance in 8 TeV data*. Tech. rep. CMS-PAS-JME-12-002. Geneva: CERN, 2013. URL: <https://cds.cern.ch/record/1543527>.
- [49] Richard C. Gray et al. “Backgrounds to Higgs Boson searches from $W\gamma^* \rightarrow \ell\nu\ell(\ell)$ asymmetric internal conversion”. In: (2011). arXiv: [1110.1368v1 \[hep-ph\]](https://arxiv.org/abs/1110.1368v1).
- [50] Thomas Junk. “Confidence Level Computation for Combining Searches with Small Statistics”. In: *Nucl. Instrum. Meth.* A434 (1999), pp. 435–443. DOI: [10.1016/S0168-9002\(99\)00498-2](https://doi.org/10.1016/S0168-9002(99)00498-2). arXiv: [hep-ex/9902006](https://arxiv.org/abs/hep-ex/9902006).
- [51] A. L. Read. “Modified frequentist analysis of search results (the CL_s method) in “Workshop on Confidence Limits”, Eds. F. James, L. Lyons, and Y. Perrin”. In: (2000). p. 81. URL: <http://cds.cern.ch/record/451614>.
- [52] A. L. Read. “Presentation of search results: The CL(s) technique”. In: *J. Phys. G* 28 (2002), p. 2693. DOI: [10.1088/0954-3899/28/10/313](https://doi.org/10.1088/0954-3899/28/10/313).
- [53] CMS Collaboration. *CMSSW*. 2016. URL: <https://cms-sw.github.io/> (visited on 03/23/2016).
- [54] R. Brun and F. Rademakers. “ROOT: An object oriented data analysis framework”. In: *Nucl. Instrum. Meth.* A389 (1997), pp. 81–86. DOI: [10.1016/S0168-9002\(97\)00048-X](https://doi.org/10.1016/S0168-9002(97)00048-X).